ORIGINAL PAPER

Experimental Study on Mechanical Behavior and Brittleness Characteristics of Longmaxi Formation Shale in Changning, Sichuan Basin, China

Sheng-Qi Yang[1] · Peng-Fei Yin[1] · P. G. Ranjith[1,2]

Abstract

At present, shale gas plays a significant role in hydrocarbon reservoirs. Hydraulic fracturing is generally employed in the exploration and exploitation of shale gas. Economic and efficient hydraulic fracturing, known as volume fracturing, is largely associated with formation characteristics, including anisotropy and brittleness in rocks. Further research on the mechanical properties of rocks, particularly the anisotropy and brittleness behavior of shale, using hydraulic fracturing would be of practical significance. In this study, shale specimens were collected from an outcrop of the lower Silurian Longmaxi formation at Sichuan Basin in southwestern China, which is the most significant exploration area for unconventional gas in China. To better understand the size, type, and shape of brittle minerals, the matrix type (and rock texture), mineral composition, and microstructure of the shale matrix were tested through X-ray diffraction analysis and scanning electron microscopy. Furthermore, the anisotropic behavior of shale specimens, including strength, deformation, and failure behaviors, was tested and analyzed under conventional triaxial compression. In addition, the brittleness characteristics of shale specimens at different bedding inclinations under different confining pressures were analyzed based on the stress–strain curve characteristic and energy balance. Different brittleness indices, including a new one proposed in this study, were used to evaluate the brittleness of shale. The impacts of anisotropy and confining pressure on brittleness were discussed in detail. When compared with other brittleness indices, the proposed brittleness index demonstrates improved effectiveness and reflects the impact of confining pressure on brittleness significantly well. The relationship between brittleness and the failure mode was revealed using the new brittleness index, and the decreasing order of brittleness was concluded as follows: tensile splitting along bedding plane mode > tensile splitting through bedding plane mode > shear along bedding plane mode > shear through bedding plane mode.

Keywords Shale gas · Rock anisotropy · Energy transformation · Brittleness index · Anisotropy of brittleness

List of Symbols

A, B	Material parameters of Saeidi criterion
B_j	Material parameters of Ramamurthy criterion
C	Cohesion
D	Diameter of specimen
E	Elasticity modulus
$E[\sigma^t]$	Expectation of tested values

H	Height of specimen
L_1, L_2, L_3	Displacements of LVDTs
M	Post-peak elastic modulus
m, s	Material parameters of Hoek–Brown criterion
R^2	Coefficient of determination
U_{ei}	Ideal elastic energy
U_{et}	Total elastic energy
U_p	Plastic energy
U_{er}	Residual elastic energy
U_a	Additional energy
U_r	Rupture energy
U_{ec}	Consumed elastic energy
v	Poisson's ratio

Greek Symbols

α	Strength reduction parameter with regard to the rock anisotropy
α_j	Material parameters of Ramamurthy criterion

✉ Sheng-Qi Yang
  yangsqi@hotmail.com

1 State Key Laboratory for Geomechanics and Deep Underground Engineering, School of Mechanics and Civil Engineering, China University of Mining and Technology, Xuzhou 221116, China

2 Deep Earth Energy Research Laboratory, Department of Civil Engineering, Monash University, Melbourne, VIC 3800, Australia

β	Bedding inclination
$\varepsilon_{1p}, \varepsilon_{3p}$	Axial strain and radial strain at peak axial deviatoric stress
$\varepsilon_e, \varepsilon_p$	Elastic deformation and plastic deformation before peak
$\varepsilon_{vd}, \varepsilon_{1d}$	Volumetric strain and axial strain of crack damage threshold
σ_o	Deviatoric stress at beginning of the elastic deformation stage
$\sigma_1, \sigma_2, \sigma_3$	Principal stresses ($\sigma_1 > \sigma_2 = \sigma_3$ conventional triaxial compression test)
σ_c	Uniaxial compressive strength (UCS)
$\sigma_{c\beta}$	UCS of intact anisotropic rock at anisotropy orientation β
σ_{ci}	UCS of intact rock
σ_{cj}	UCS at a particular anisotropy orientation
σ_d	Crack damage threshold
σ_{de}	Axial deviatoric stress
σ_p	Peak axial deviatoric stress
σ_r	Residual strength
σ_i^t, σ_i^p	Tested and predicted values of σ for the ith data
φ	Internal friction angle

1 Introduction

Shale is a widely distributed sedimentary rock in the earth's crust, most of which contains rich organic matter, and plays a significant role in hydrocarbon reservoirs. At present, shale gas has become a strategically and globally significant unconventional resource. Hydraulic fracturing is generally employed in the exploration and exploitation of shale gas. The economic and efficient method of hydraulic fracturing is to create more complex fracture networks, known as volume fracturing. However, this method is largely employed to study formation characteristics, including stress diversity factor, rock elastic properties, rock anisotropy and heterogeneity, distribution of natural fractures, and the brittleness of rocks (Chen et al. 2017). It is observed that mechanical properties such as the long horizontal section, high bedding development of rock formation, and high hardness and brittleness of rocks can make the borehole walls of shale gas prone to collapse, leakage, and other grave instability problems. Therefore, further research on the mechanical properties of rocks, particularly the anisotropy and brittleness behavior of shale, is of practical significance for applying hydraulic fracturing in the exploration and exploitation of shale gas.

Shales are well known for their distinct anisotropy of mechanical properties. Understanding the anisotropic behavior of shale would have an essential bearing on shale gas exploration, wellbore stability, interpretation of microseismic monitoring, and so on. Several previous research studies have explored the anisotropic behavior of shale—Niandou et al. (1997) and Masri et al. (2014) conducted experiments on Tournemire shale; Kuila et al. (2011) researched low-porosity shales from the Officer Basin in Western Australia; Cho et al. (2012) and Kim et al. (2012) studied Boryeong shale; Yang et al. (2019) analyzed Changsha shale. Furthermore, Josh et al. (2012), Heng et al. (2015), Rybacki et al. (2015), Wu et al. (2017), and Li et al. (2017) have also investigated the mechanical behavior of shale rocks. Similarly, several other types of anisotropic rocks have also been studied—Nasseri et al. (1997, 2003) studied schists, Hakala et al. (2007) explored gneiss, and Yin and Yang (2018) examined layered sandstone. Of particular importance is Ramamurthy's classification (1993) of the anisotropy of rocks into three groups, namely, "U" type, undulatory type, and "shoulder" type. Simultaneously, various failure criteria have been proposed to describe the strength anisotropy of anisotropic rocks. The first attempt seems to be the single weakness plane theory proposed by Jaeger (1960), followed by studies conducted by Hoek and Brown (1980), Ramamurthy et al. (1988), Rao et al. (1986), Tien and Kuo (2001), Saeidi et al. (2013, 2014), Singh et al. (2015), and Shi et al. (2016). In these studies, the mechanical properties of anisotropic rocks were researched, and the strength and failure behavior were reported. On the other hand, many mechanical models based on damage theory were proposed for anisotropic rocks by a series of researches: Chen et al. (2010, 2012) proposed a coupled elastoplastic damage model to describe the strongly anisotropic sedimentary, and studied the plastic deformation and induced damage in sedimentary rocks with structural anisotropy; Yao et al. (2016) conducted a numerical study of damage and failure in anisotropic cohesive brittle materials rocks; Qi et al. (2016a, b) proposed a numerical micro-mechanical damage model for modeling of induced damage in an initially anisotropic material, and a three dimensional micro-mechanical model was developed for modeling micro-crack growth and plastic frictional sliding in initially anisotropic quasi-brittle materials. These models based on damage theory show good capability to reproduce the main features of mechanical behavior of strong anisotropic rocks; however, it needs to be verified by more experimental data for different types of anisotropic rocks in the following studies. Owing to difficulties faced in specimen preparation, there has been little research on shale with various bedding inclinations. Therefore, shale specimens with various bedding inclinations are required to further investigate the anisotropic behavior.

In rock engineering applications, brittleness is a term commonly used to identify the possible failure characteristics of the rock mass (Zhang et al. 2016). For implementing hydraulic fracturing, higher the brittleness of reservoirs, deeper the fractures will extend, more complex the fractures will be, and higher the single well productivity will

be. Therefore, the evaluation of brittleness is a major challenge and plays an essential role in petroleum engineering. To date, several different expressions have been proposed to quantify the brittleness of rocks. For instance, Morley (1944) and Hetényi (1950) defined brittleness as the lack of ductility; Obert and Duvall (1967) defined it as material failure by fracture at or only slightly beyond the yield stress; Ramsey (1968) defined it as the destruction of internal cohesion; Howell (1960) defined it as a property of rock material rupture or fracture with small or no plastic flow; Tarasov and Potvin (2013) defined it as a self-sustaining failure process. However, there is still no unique definition, concept, or measurement for brittleness. According to a summary by Hucka and Das (1974) and Zhang et al. (2016), with increase in brittleness, brittle rocks may commonly exhibit the following characteristics: (1) low values of elongation of grains, (2) fracture failure, where distinct failure fracture surfaces can be observed during brittle failure (such surfaces cannot be observed in ductile rocks upon failure), (3) higher ratio of compressive to tensile strength, (4) higher toughness, (5) higher angle of internal friction, (6) formation of cracks in indentation, (7) higher resilience resulting from the larger elastic proportion, (8) greater percentages of brittle minerals such as quartz and minimal amounts of ductile minerals such as clay minerals, (9) higher Young's modulus and lower Poisson's ratio values, (10) huge strength reduction occurs with failure, (11) intensive failure process, wherein the brittle rocks fail suddenly in an intensive and self-sustaining way.

The brittleness index (BI) is a term that is usually used to quantify the brittleness of rock mass, and several different definitions of BI have been recommended so far. To measure brittleness, various influencing factors should be taken into consideration, including mineral composition, in situ stress, and strength parameters. To date, several different ways of expressing the brittleness of rocks have been proposed to quantify its extent (Hucka and Das 1974; Altindag 2002; Hajiabdolmajid et al. 2003; Nygård et al. 2006; Rickman et al. 2008; Yagiz 2009; Holt et al. 2011; Tarasov and Potvin 2013; Jin et al. 2014a, b). These BI definitions are based mainly on approaches including the stress–strain curve, uniaxial compressive strength and Brazilian tensile strength, penetration, impactor hardness tests, mineral composition, porosity and grain size, and geophysical methods. Table 1 summarizes some of the universal BI definitions, mainly considering four approaches. Mineral composition is very easy to obtain and can be determined precisely by conducting laboratory analysis such as X-ray diffraction (XRD) testing. In fact, methods based on strength parameters, stress–strain characteristics, and energy balance analysis are all determined by stress–strain curve, in which strength, deformation, and energy balance parameters can

Table 1 Summary of some universal BI definitions

Test method	Formulae	References	Remarks
Mineral composition	$BI_1 = W_Q/W_{Q+C+Cl}$	Jarvie et al. (2007)	W_x = weight fraction of component x; Q = quartz; C = carbonate; Cl = clay; Dol = dolomite; TOC = total organic carbon; QFM = quartz + feldspar + mica
	$BI_2 = (W_Q + W_c)/W_{total}$	Rickman et al. (2008)	
	$BI_3 = W_{QFM+C}/W_{total}$	Jin et al. (2015)	
Strength parameters	$BI_4 = \sigma_c/\sigma_t$	Hucka and Das (1974)	σ_c = uniaxial compressive strength; σ_t = Brazilian tensile strength; φ = internal friction angle; ρ = density
	$BI_5 = (\sigma_c - \sigma_t)/(\sigma_c + \sigma_t)$		
	$BI_6 = \sin(\varphi)$		
	$BI_7 = \sigma_c\sigma_t/2$	Altindag (2002)	
	$BI_8 = 0.198\sigma_c - 2.174\sigma_c + 0.913\rho - 3.807$	Yagiz (2009)	
Stress–strain characteristics	$BI_9 = \varepsilon_p \times 100\%$	Andreev (1995)	ε_p = sustained plastic strain at failure; ε_e = total elastic strain; ε_f = total strain at failure; ε_r = residual strain; σ_f = stress at failure; σ_r = residual strength
	$BI_{10} = (\sigma_f - \sigma_r)/\sigma_f$	Bishop (1967)	
	$BI_{11} = \varepsilon_e/\varepsilon_f$	Hucka and Das (1974)	
	$BI_{12} = (\varepsilon_f - \varepsilon_r)/\varepsilon_f$	Andreev (1995)	
Energy balance analysis	$BI_{13} = U_{et}/(U_{et} + U_p)$	Hucka and Das (1974)	U_{et} = total elastic energy; U_p = plastic energy; U_r = rupture energy; U_{ec} = consumed elastic energy; U_a = additional energy; E = elastic modulus; M = post-peak modulus
	$BI_{14} = U_r/U_{ec} = (M - E)/M$	Tarasov and Potvin (2013)	
	$BI_{15} = U_a/U_{ec}$		
	$BI_{16} = U_{et}/(U_r + U_p)$	Munoz et al. (2016)	
	$BI_{17} = (U_{et} + U_p)/(U_r + U_p)$		
	$BI_{18} = U_{et}/U_r$		
	$BI_{19} = (U_r + U_p)/(U_{ec} + U_p)$	Ai et al. (2016)	
	$BI_{20} = U_a/(U_{ec} + U_p)$		

be obtained. The use of stress–strain curves to determine strength parameters is common in rock mechanics, as they can be obtained easily using the triaxial compression test. The brittleness of material is a type of mechanical response to external stress conditions. For a material specimen, the composition and internal structure are constant and the brittleness can be different if different stress conditions are applied. Therefore, the specific stress condition encountered by the rock must be considered when its brittleness is evaluated. Thus, BI definitions based on stress conditions are more significant.

In this study, shale specimens were collected from an outcrop of the lower Silurian Longmaxi formation at Sichuan Basin of southwestern China, which is the most significant exploration area of unconventional gas in the country. To better understand the type and shape of brittle minerals, matrix type, and finally rock texture, the mineral composition and microstructure of the shale matrix were tested through XRD and scanning electron microscopy (SEM). Furthermore, the anisotropic behavior of shale specimens, including the strength, deformation, and failure behaviors, was tested and analyzed under conventional triaxial compression. Furthermore, the brittleness characteristics of the shale specimens were analyzed at various bedding inclinations under various confining pressures, based on the stress–strain curve and energy balance. Various brittleness indices, including a new one proposed in this research, were used to evaluate the brittleness of shale. The impact of anisotropy and confining pressure on brittleness were investigated in detail.

2 Shale Sampling and Its Characterization

2.1 Geologic Setting and Shale Sampling

The marine stratum area in southern China has excellent geological settings for shale gas accumulation, leading to the formation of rich shale gas resources. Shale gas is expected to become a strategically significant replacement for China's existing oil and gas resources. The China Geological Survey has observed that the high-quality shale of the Longmaxi formation in the middle and upper Yangtze regions has a wide distribution, high thickness, and huge hydrocarbon resource potential, accounting for 20% of the shale gas resources in China. Figure 1a depicts the main exploratory shale gas wells at lower Silurian Longmaxi formation (adopted from China Geological Survey). The Sichuan Basin of southwestern China, which has an area of 180,000 km^2, is the most significant exploration area of unconventional gas in the country. Therefore, studying the shale in this area is of higher significance.

As depicted in Fig. 1b, the shale specimens tested in this research are taken from a quarry in the Changning area,

Sichuan, China, from which the linear distance to the Ning-201 shale gas well is approximately 30 km. Because of excavation, there are a large number of fresh and intact shale outcrops here, and it is very convenient for collection. The sampling site is located in the southern edge of the Sichuan Basin. This area is rich in shale deposits, which, according to geology, belongs to the lower Silurian Longmaxi formation, Paleozoic of the middle and upper Yangtze regions. This shale is a marine black shale with evident bedding development. It was formed in a deep-water continental shelf facies sedimentary controlled by continental margin depression in a water depth of approximately 200 m, with abundant biological fossils and a strong reduction environment. It is rich in organic matter, including graptolite fossils and authigenic pyrite.

Figure 2a shows the fresh and intact shale blocks taken from the outcrop. To ensure the integrity and homogeneity of the shale specimens used in laboratory tests, the following criteria are followed for sampling:

1. The volume of the block should be moderate. Too large a volume is not conducive to transportation and indoor processing; on the contrary, too small a volume cannot guarantee sufficient quantity of specimens in one block.
2. The blocks should be as complete as possible without cracks to ensure the integrity and homogeneity of the processed specimens.
3. The bedding of the rock blocks should be distinct. The bedding should also be horizontal when the rock mass is laid flat to facilitate the indoor processing of specimens with different bedding inclinations.

Figure 2b shows how shale blocks are drilled into cylindrical specimens with different bedding inclinations. The bedding inclination in this research is defined as the angle between the bedding plane and the end face of the cylindrical specimen, represented as β. By varying the placement inclination of the block, shale specimens with seven sets of bedding inclinations are drilled, at $\beta = 0°$, 15°, 30°, 45°, 60°, 75°, and 90°. After drilling, as shown in Fig. 2c, the specimens were processed into standard specimens with dimensions 50 mm × 100 mm, using the method suggested by ISRM (International Society for Rock Mechanics 2007). All the prepared specimens are placed at a room temperature of 20 ± 0.5 °C and humidity of 65% ± 5% and tested within 30 days.

2.2 Mineral Composition Analysis

The minerals in shale contain mainly quartz, feldspar, calcite, and clay, in which the clay includes kaolinite, montmorillonite, illite, hydromica, and so on. In general, the mineral composition of shale varies with the depths and
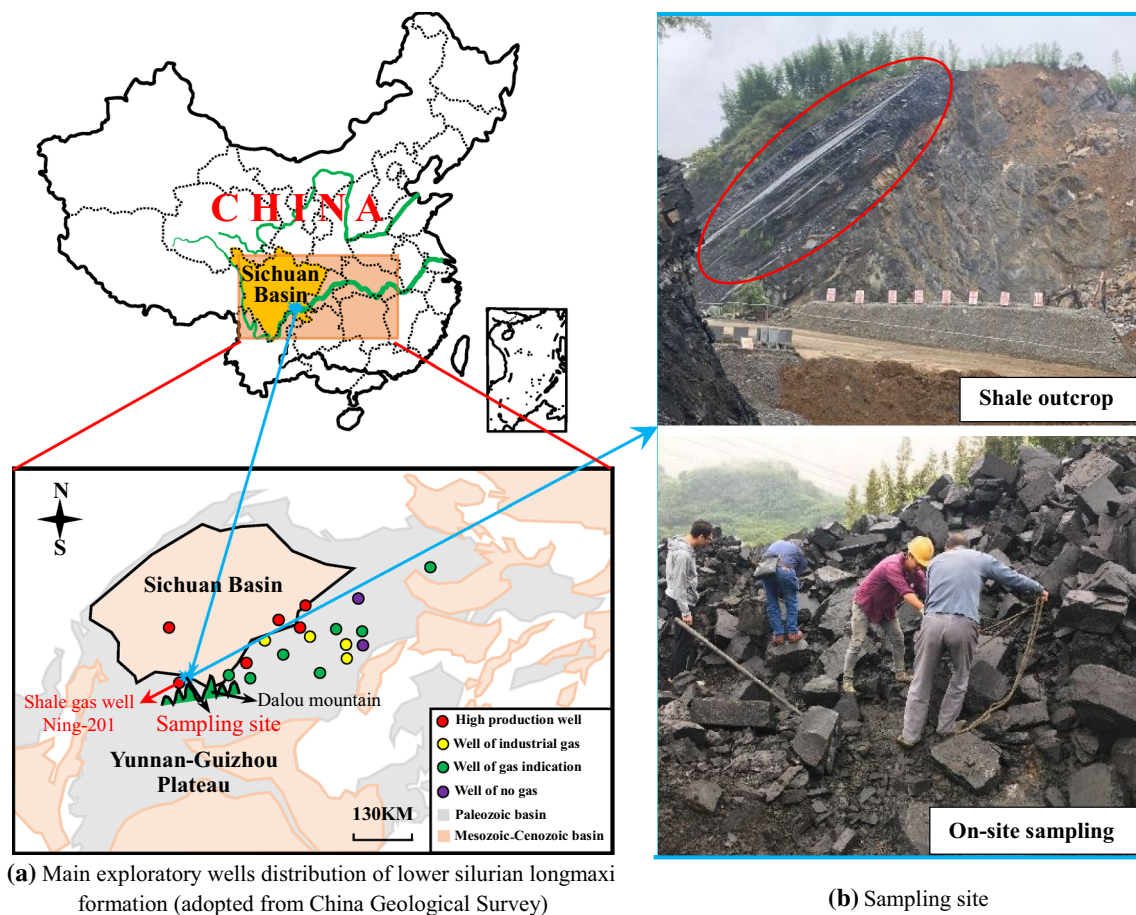
(a) Main exploratory wells distribution of lower silurian longmaxi formation (adopted from China Geological Survey)

(b) Sampling site

Fig. 1 Geological settings and sampling site of shale specimens tested in this research

(a) Shale blocks used for drilling **(b)** Schematic diagram of shale specimen drilling **(c)** Prepared shale specimens
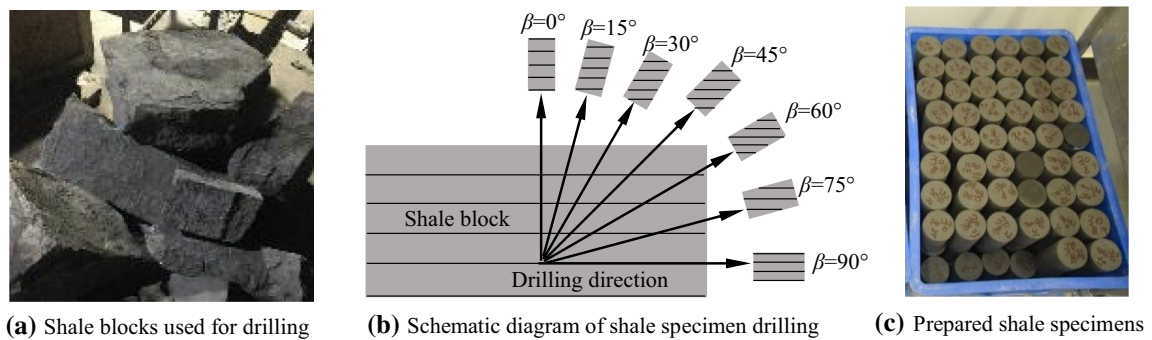
Fig. 2 Preparation diagram of shale specimens at different bedding inclinations

locations, which can lead to different properties. On the other hand, quartz has a distinct impact on the degree of brittleness of shale, which is a key factor impacting the development of hydraulic fractures in shale reservoirs. Figure 3 presents the XRD test result of shale specimens in this research, indicating the mineral composition and proportion of shale specimens. From Fig. 3, it can be seen that this shale specimen contains mainly quartz, calcite,

Fe-muscovite, and clay, and other minerals such as plagioclase, potash feldspar, and pyrite are present in very small amounts. The clay in this shale specimen mainly contains illite, chlorite, and illite/smectite (I/S) formation. The proportion of quartz plus calcite is 63.9%, which is a large part of the mineral composition, indicating the high brittleness of this shale specimen.

Fig. 3 Mineral composition of Shale specimen in this research

(a) Mineral composition and proportion

(b) Clay composition and proportion
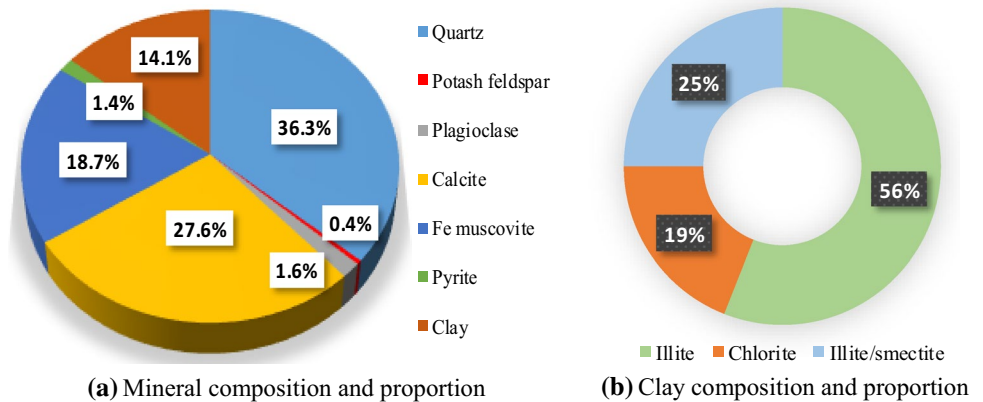
2.3 Microstructure Analysis

As a typical sedimentary rock, shale has a very fine pore structure and fracture network because of its fine mineral grains. The micropores and microfractures inside or between mineral grains will be different according to their types, which can lead to differences in mechanical behavior at the macroscopic level. Figure 4 shows the SEM images of the shale specimen surface. From Fig. 4a, it can be clearly observed that a large number of mineral grains and debris supporting each other and overlapping, squeezed together, and forming different shapes of skeleton pores. The clay minerals in the sheet can easily become highly deformed by getting squeezed with other mineral grains. Thus, a large number of pores are formed at the edge of these mineral grains. In Fig. 4b, some clay minerals and pyrite grains can be observed. The clay minerals in the sheet have interlayer micropores formed by clay crystal layers. Pyrite is composed of many pyrite grains in the strawberry-like aggregate, and there are a number of micropores between these grains.

3 Methodology

3.1 Conventional Triaxial Compression Test

This test is aimed at identifying the anisotropic characteristics of compression strength, deformation, and failure mode of the shale specimens, further, at establishing new method for the evaluation of shale brittleness, which combines the strength parameters and stress–strain curve characteristics.

Conventional triaxial compression tests were performed on the multifunctional triaxial test system for rocks at the State Key Laboratory for Geomechanics and Deep Underground Engineering, China University of Mining and Technology. The maximum axial loading capacity of the servo-controlled system is 400 MPa and the maximum confining
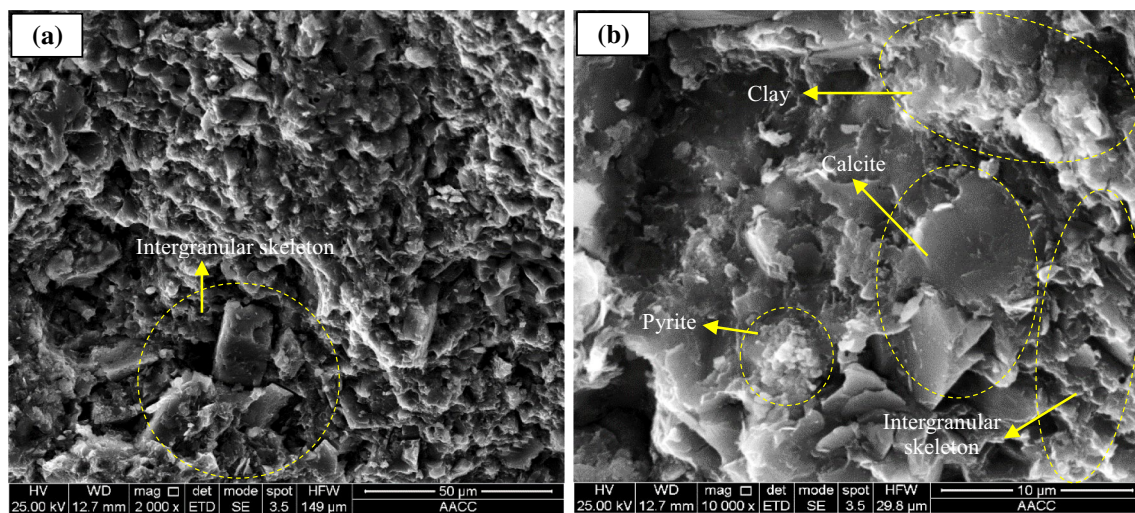
Fig. 4 SEM images of shale specimen in this research

pressure loading capacity is 60 MPa. During the tests, the axial deformation was measured by two axial linear variable differential transducers (LVDTs) with a range of 10 mm. The radial deformation was measured by an LVDT which is in hoop with a range of 6 mm.

All the tested specimens were standard cylinders 50 mm in diameter and 100 mm in height, as shown in Fig. 5. Axial loading occurs in the displacement loading mode, whereas the confining pressure occurs in the stress loading mode. The specimens were divided into seven groups based on their bedding inclinations $\beta = 0°$, 15°, 30°, 45°, 60°, 75°, and 90° and tested under five different confining pressures ($\sigma_2 = \sigma_3$) of 0, 5, 10, 15, and 20 MPa. First, the confining pressure was increased to the desired value at a constant rate of 8 MPa/min (this rate ensures that the loading is slow enough and will not damage the specimen); second, axial deviatoric stress was applied to the specimens at a constant axial displacement rate of 0.05 mm/min (this rate ensures that the specimens are tested under quasi-static loading); when the specimens reached their residual strengths or completely lost their carrying capacities, the loading was stopped and the experiment ended. All the experiments were performed at a room temperature of 20 ± 0.5 °C and humidity of $65\% \pm 5\%$ within 10 days.

The experimental data were recorded by the system automatically, including axial deviatoric stress σ_{de}, confining pressures σ_3, axial displacements L_1 and L_2 by two axial LVDTs, and the radial displacement L_3 by one axial LVDT. The mass and geometry of each specimen were measured and recorded before the experiments; D is the diameter and H is the height.

From the tested stress–strain curves, mechanical parameters can be obtained. Figure 6 depicts the stress stages in the stress–strain curve under compression. It also illustrates how the basic strength and deformation parameters are calculated. As can be observed from Fig. 6, three stress stages can be observed before the peak, characterized as porosity
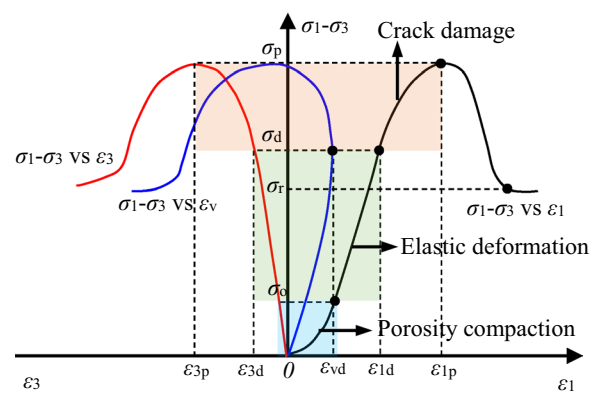

Fig. 6 Different stress stages in stress–strain curve under triaxial compression

compaction, elastic deformation, and crack damage, with increase in the deviatoric stress. In the stage of porosity compaction, the initial microcracks in the rock are compacted and σ_o is the deviatoric stress, which defines the end of this stage and the beginning of the elastic deformation stage. It is considered that no new damages or microcracks are initiated in the elastic deformation stage; therefore, the elasticity modulus E is calculated using the average slope in the range of elastic deformation and Poisson's ratio v is obtained using the average of the absolute value of the ratio of radial strain and axial strain in the range of elastic deformation. With increase in loading up to the stage of crack damage, new damage and microcracks initiate and extend in the rock, and plastic deformation commences. As shown in Fig. 6, at the beginning of this stage, the volumetric deformation switches from compaction dominated to dilatancy dominated. The crack damage threshold (σ_d) of the specimen (Wong et al. 1997; Fairhurst and Hudson 1999; Heap et al. 2009; Yang et al. 2015, 2017) is the corresponding axial deviatoric stress at this switch point. ε_{vd} and ε_{1d} are the volumetric strain and axial strain at the switch point. σ_p
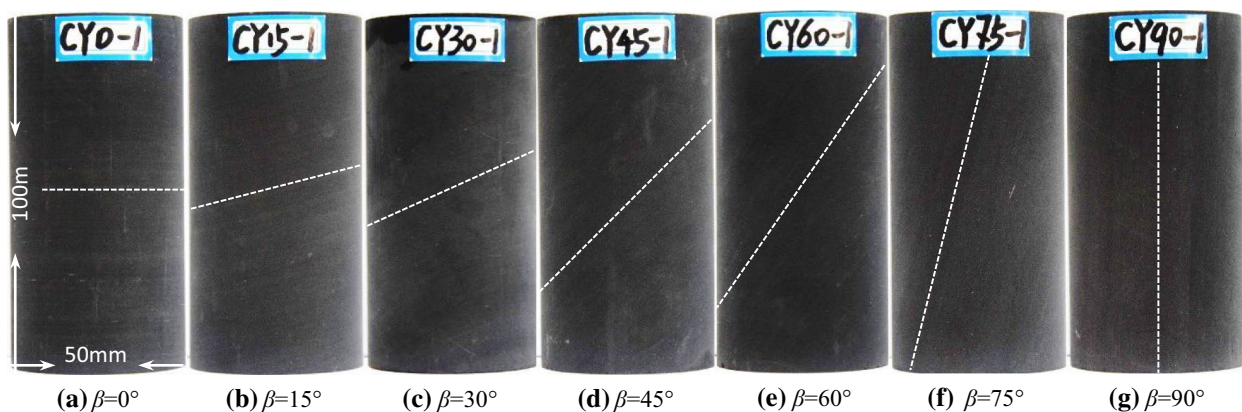

Fig. 5 Cylinder shale specimens at different bedding inclinations

is the peak axial deviatoric stress that is also defined as the failure strength of the specimens. ε_{1p} and ε_{3p} are defined as the axial strain and radial strain upon reaching the peak axial deviatoric stress. σ_r is the residual axial deviatoric stress that is also defined as the residual strength.

3.2 Evaluation Approaches for Shale Brittleness

As it was stated in the Introduction, the brittleness index is a term that is usually used to quantify the brittleness of rock mass. Table 1 provides a summary of the previous BI definitions. These various BI definitions indicate that the brittleness of rocks is complicated and hard to quantize uniformly. A specific BI definition may work very well for some types of rocks or some specific stress conditions. However, it may not work well under another condition. For the laboratory investigation, several tests can be used to obtain the BI of the rock specimen. In this study, BI definitions, which have been proposed based on mineral composition, stress–strain curve parameters, and energy balance is considered to evaluate the brittleness of shale specimens.

1. Approaches based on mineral composition

The mineral composition of the shale specimens used in this research has been tested and analyzed by XRD in Sect. 2.2. The mineral percentage is shown in Fig. 3. Based on the result, BI_1, BI_2, and BI_3 are used to evaluate the brittleness of shale specimens used in this research. For BI_1, BI_2, and BI_3, larger the value is, more brittle mineral content the rock specimen has and higher its brittleness is. It should be noted that for the same rock specimens, their brittleness indexes are constant when they are characterized by the content of brittle minerals; however, they exhibit varying brittleness characteristics under different stress conditions.

2. Analysis of stress–strain curve parameters

For brittle rock, elastic deformation often accounts for a significant proportion of the entire deformation, and little plastic deformation occurs before failure. In general, plastic deformation is the accumulation of internal damage, which indicates that instability failure for brittle rocks occurs rapidly once damage inside the rock appears. In this study, BI_{10} is used to characterize the brittleness of the shale specimen. BI_{10} reflects the relative magnitude of recoverable deformation to the magnitude of total deformation at failure. Larger the value of BI_{10}, lower the plastic deformation when the rock specimen fails, which indicates that the rock specimen has higher brittleness.

3. Analysis based on energy balance

The rock failure process is essentially a process of balancing energy absorption and release. As shown in Fig. 7, the energy evolution of the rock failure process can be clearly illustrated based on stress–strain curves. The rock specimen constantly absorbs external energy before failure, which causes a significant amount of elastic energy (in green color) to be stored in the rock. Simultaneously, some other energies are dissipated (in the shadowed area) owing to the occurrence of internal damage, which is reflected by the unrecoverable plastic deformation in the stress–strain curve. When the rock fails, the stress reduces and the energy stored in the rock starts to release. The release of elastic energy leads to crack propagation and macro-fractures in the specimens, and the rock specimens cannot absorb further energy and are damaged. In this study, BI_{13}, BI_{14}, BI_{15}, BI_{16}, BI_{17}, BI_{18}, BI_{19}, and BI_{20} are used to characterize the brittleness of the shale specimen. Using various brittleness indexes, the various definitions based on energy balance are compared and the comprehensive brittleness of the shale specimens can be ascertained. Figure 7 reveals that the plastic and rupture energies are the key to determine the degree of brittleness. For brittle rock material, very less plastic energy accumulates at the peak. Similarly, rupture energy is rare

Fig. 7 Energy evolution of rock failure process on stress–strain curve

Springer
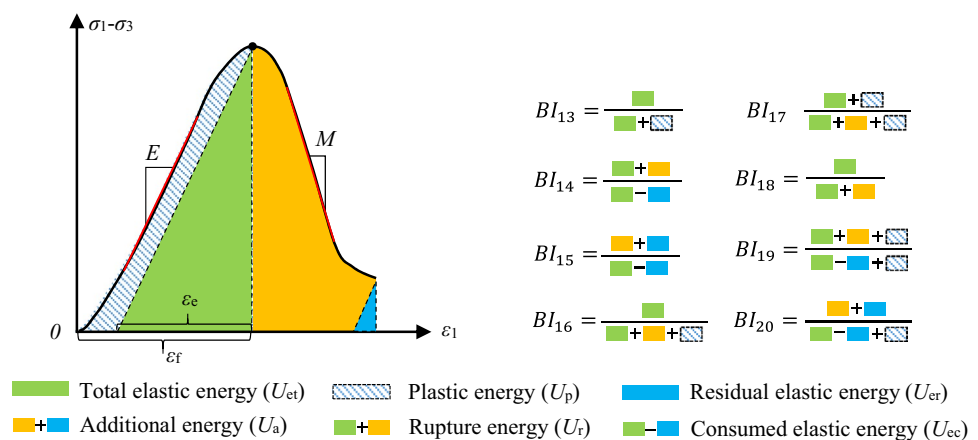
as well, because the associated stress drops sharply to a low level when brittle failure occurs. In Fig. 7, E is the elasticity modulus before the peak, which is calculated by the average slope in the range of elastic deformation. M is the post-peak elastic modulus, which is calculated by the average slope in the range of post-peak deformation. E can help to determine the magnitude of elastic strain and elastic energy.

4 Analysis of Mechanical Characteristics

4.1 Analysis of Stress–Strain Curves

To investigate the anisotropic behavior of shale, specimens at seven bedding inclinations were tested. Figure 8 shows the deviatoric stress–strain curves of shale specimens under different confining pressures. Owing to space limitations, specimens only at the bedding inclinations of 0°, 45°, and 90° were presented. From Fig. 8, it can be revealed that the confining pressure has a distinct impact on the failure strength. Furthermore, the shapes of their stress–strain curves clearly reveal that the specimens experienced little plastic deformation in the pre-peak region and reached the failure point in a sharp curve type, which indicates that the specimens exhibit strong brittle behavior even under a certain confining pressure.

Figure 9 shows the axial deviatoric stress–strain curves of shale specimens under different bedding inclinations. Owing to space limitations, specimens only under the confining pressures of 0, 10, and 20 MPa were presented. From the curves under each confining pressure, it can be clearly seen that specimens with different bedding inclinations exhibit different mechanical characteristics; for instance, failure strength and Young's modulus show apparent changes with respect to the bedding inclination. This indicates that the shale specimens in this research have a distinct anisotropy in mechanical behavior. On the other hand, the specimens also show distinct brittleness as the stress drops steeply after reaching the peak point. However, under the confining pressures of 10 and 20 MPa, specimens at $\beta = 30°$ and 75° show low brittleness, and the stress drops slowly after the peak point. This indicates that the brittleness is also anisotropic. Further details will be discussed in the following sections.
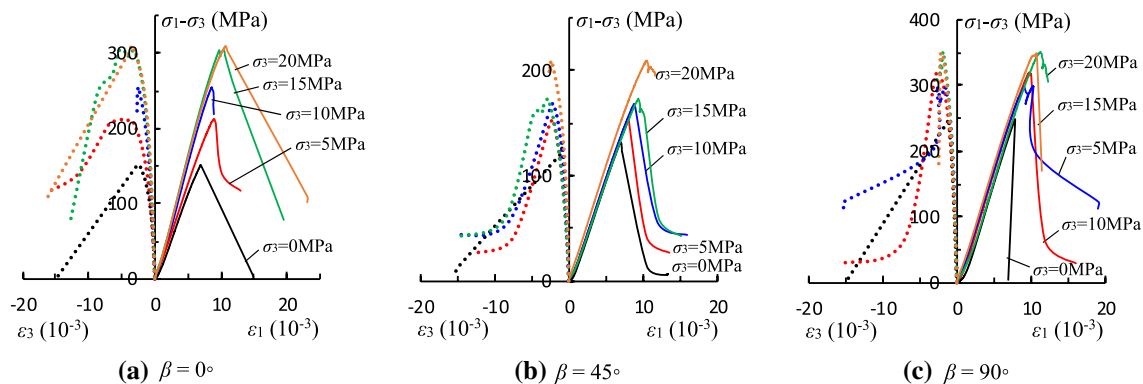

Fig. 8 Deviatoric stress–strain curves of shale specimens under different confining pressures
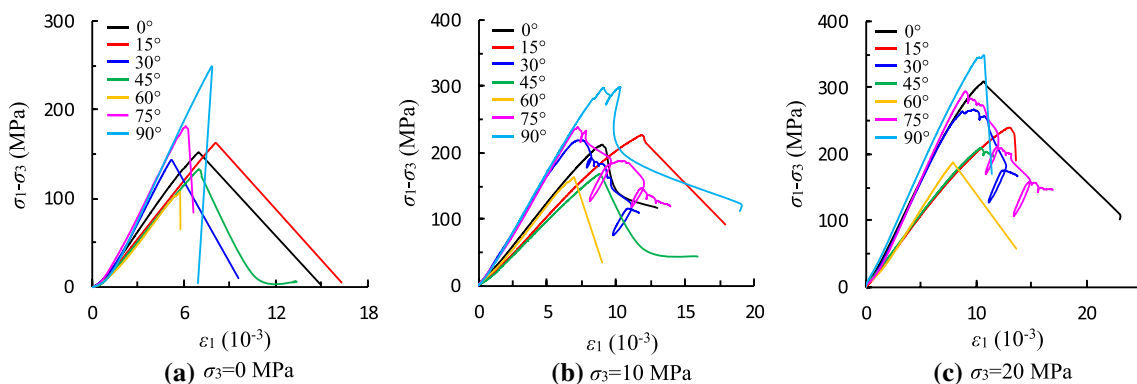

Fig. 9 Axial deviatoric stress–strain curves of shale specimens under different bedding inclinations

4.2 Strength and Deformation Behavior

In relation to the stress–strain curves presented in Figs. 8 and 9, significant mechanical characteristics of the tested specimens have been evaluated. Their variation with respect to the bedding inclinations are plotted in Fig. 10a–e. Furthermore, the apparent cohesion C and internal friction angle φ of shale specimens at different bedding inclinations are calculated according to the Mohr–Coulomb criterion and the variations with respect to the bedding inclinations are plotted in Fig. 10f.

From Fig. 10a, b, it can be observed that the peak strength (σ_p) and crack damage threshold (σ_d) all display "U"-type variation trends with respect to the bedding inclination under each confining pressure. All the maximum values are observed at $\beta = 90°$ and almost all the minimum values are observed at $\beta = 45°$ and 60°. From Fig. 10c, the peak axial strain (ε_{1p}) appears to be wavy and to be increasing with the increase in the bedding inclination, which does not seem to be a distinct variation pattern. The peak axial strain depends on the peak strength and deformation modulus. Both high peak strength and low deformation modulus can lead to large peak axial strain. As depicted in Fig. 10d, the elasticity modulus (E) shows "W"-type variation trends with respect to the bedding inclinations, the three crest values are observed at

$\beta = 0°$, 30°, and 75°–90°, whereas the two trough values are observed at $\beta = 15°$ and 45°. Combining the variations observed in peak strength (Fig. 10a) and elasticity modulus (Fig. 10d), it can be observed that the variations in peak axial strain can be illustrated clearly. When β is under 60°, the peak strength decreases with respect to the bedding inclination and the elasticity modulus is undulant. As a consequence, the peak axial strain is of undulatory type as well, and each crest or trough value is smaller than the previous one. When β is above 60°, the peak strength and elasticity modulus increase with respect to the bedding inclination. However, the peak strength at 60° is the minimum and the elasticity modulus is not large enough; as a consequence, the peak axial strain is minimum at 60°. In Fig. 10e, f, Poisson's ratio (v) and the apparent friction angle (φ) show no particular pattern with the increase in the bedding inclination. Moreover, the apparent cohesion (C) value displays a "U"-type with the increase in the bedding inclination, which distinctly indicates anisotropic behavior of the shale specimen. It is well known that cohesion can be regarded as the shear strength of the failure plane with normal stress, which means it is closely related to the shear behavior of the specimen. At low or high bedding inclinations (0°, 15°, 90°), the bedding planes make the fracture propagation discontinuous; therefore, it is more difficult for the shear fractures to propagate through
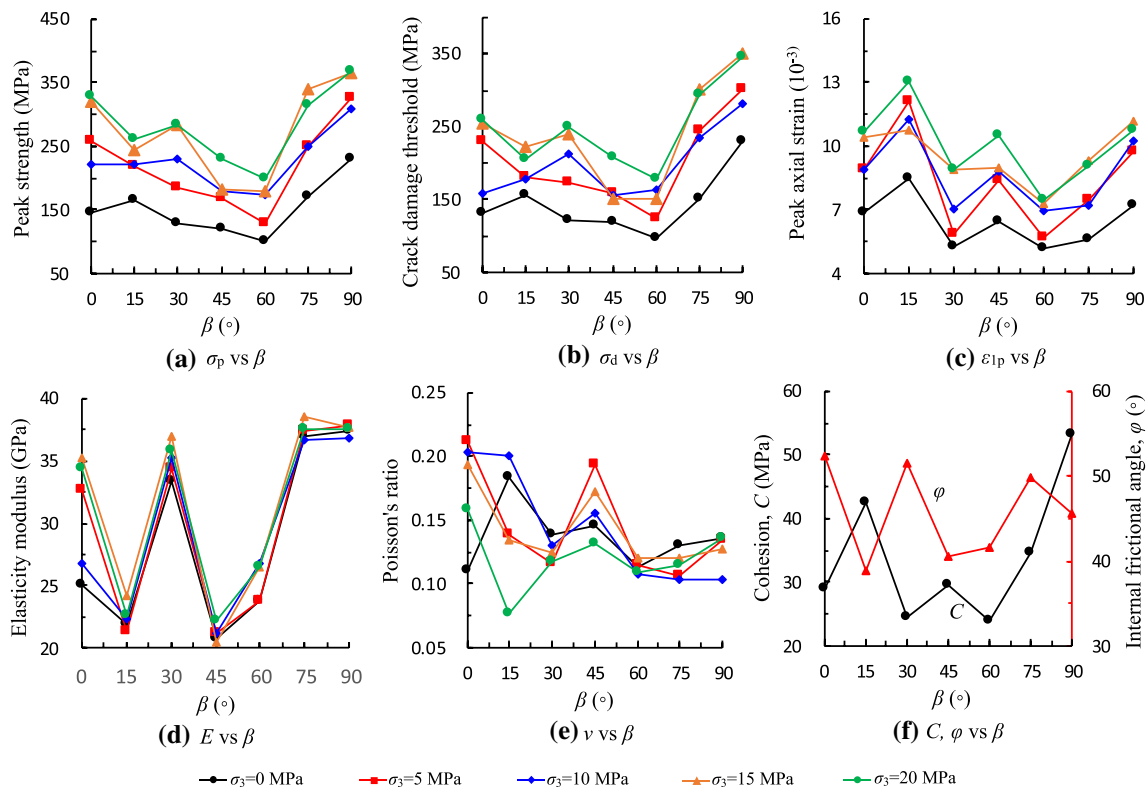
Fig. 10 Main strength and deformation parameters variation with respect to the bedding inclinations

the bedding planes, which leads to a large cohesion value. At medium bedding inclinations (30°–75°), the fracture can easily propagate along the bedding planes, which leads to a small cohesion value.

In addition to the linear Mohr–Coulomb criterion, the Hoek–Brown criterion is an empirical strength criterion that has been widely applied to describe the non-linear behavior of strength. The basic equation can be written as (Hoek and Brown 1980, 1997):

$$\sigma_1 = \sigma_3 + \sigma_c \left(m \frac{\sigma_3}{\sigma_c} + s \right)^{0.5}, \tag{1}$$

where σ_c is the uniaxial compressive strength (UCS) of the intact rock and m and s are material constants for a specific rock. When the parameter m is larger, the rock is stronger. The parameter s reflects the fractured extent of the rock, ranging from 0 to 1. When the parameter s is closer to 1, the rock is more intact. In this study, the shale specimens at each bedding inclinations were intact; therefore, the parameter m was selected as 1. By substituting the triaxial compression test data into Eq. (1), the parameters m for the specimens at each bedding inclination can be obtained, and they are listed in Table 3.

To better describe the failure strength of anisotropic rocks, various failure criteria have been proposed. Ramamurthy et al. (1988) and Saeidi et al. (2013) proposed empirical criteria. Ramamurthy et al. (1988) and Rao et al. (1986) proposed an empirical strength criterion to predict the non-linear strength behavior of intact anisotropic rocks; the empirical strength criterion can be expressed as follows:

$$\frac{(\sigma_1 - \sigma_3)}{\sigma_3} = B_j \left(\frac{\sigma_{cj}}{\sigma_3} \right)^{\alpha_j}, \tag{2}$$

where σ_1 and σ_3 are the major and minor principal stresses and σ_{cj} is the uniaxial compressive strength at the particular anisotropy orientation β. By defining the parameters α_j and B_j, the anisotropy of material strength can be considered

here, and the functions of anisotropic orientation are as follows:

$$\frac{\alpha_j}{\alpha_{90}} = \left(\frac{\sigma_{cj}}{\sigma_{c90}} \right)^{1-\alpha_{90}}, \tag{3}$$

$$\frac{B_j}{B_{90}} = \left(\frac{\alpha_{90}}{\alpha_j} \right)^{0.5}, \tag{4}$$

where σ_{c90} is the uniaxial compressive strength when $\beta = 90°$ and α_{90} and B_{90} are the values of α_j and B_j when $\beta = 90°$. In this research, by substituting the triaxial compression test data into Eq. (2), the parameters α_j and B_j at each anisotropy orientation can be calculated. The calculated parameters are listed in Table 2.

On the other hand, in a later research, Saeidi et al. (2013) modified Rafiai (2011)'s failure criterion, which is valid for isotropic rocks. In Rafiai's research, the empirical criterion is used to predict intact rock, and the empirical failure criterion under triaxial conditions is expressed as follows:

$$\frac{\sigma_1}{\sigma_{ci}} = \frac{\sigma_3}{\sigma_{ci}} + \left[\frac{1 + A(\sigma_3/\sigma_{ci})}{1 + B(\sigma_3/\sigma_{ci})} \right] - r, \tag{5}$$

where σ_{ci} is the uniaxial compressive strength of intact rock; A and B are constant parameters that depend on the properties of the rock. The parameter r is the strength reduction factor, which is considered equal to 0 for intact rock and 1 for highly jointed rock masses. To apply Rafiai's failure criterion to transversely isotropic rocks, Saeidi et al. (2013) modified the failure criterion (Eq. 5) to the following:

$$\sigma_1 = \sigma_3 + \sigma_{c\beta} \left[\frac{1 + A(\sigma_3/\sigma_{c\beta})}{\alpha + B(\sigma_3/\sigma_{c\beta})} \right], \tag{6}$$

where $\sigma_{c\beta}$ is the uniaxial compressive strength of anisotropic rock at the anisotropy orientation β and α is the strength reduction parameter considering the rock anisotropy. In this modified failure criterion, parameter r in Eq. (5) is

Table 2 Calculated parameters of different strength criteria for shale specimen in this research

β (°)	Mohr–Coulomb			Hoek–Brown			Ramamurthy			Saeidi			
	C (MPa)	φ (°)	R^2	m	s	R^2	α_j	B_j	R^{2*}	α	A	B	R^2
0	28.88	52.29	0.8085	27.5922	1	0.8145	0.7972	3.0890	0.8370	0.9564	25.7379	8.7969	0.8304
15	42.60	38.80	0.9010	10.4611	1	0.8818	0.9085	1.7362	0.9743	0.9952	40.4411	25.8536	0.9678
30	24.46	51.49	0.9399	24.1952	1	0.9661	0.7051	3.6999	0.9763	1.0151	20.9796	6.3442	0.9762
45	29.64	40.45	0.8961	11.0963	1	0.8911	0.8384	2.1623	0.8971	0.9606	8.3958	2.9193	0.8986
60	23.96	41.66	0.9409	11.9788	1	0.9596	0.7576	2.6621	0.9765	1.0171	13.6554	5.3255	0.9729
75	34.57	49.92	0.8242	21.4080	1	0.8398	0.8098	2.6894	0.8707	0.9931	29.0614	12.5093	0.8720
90	53.35	45.61	0.8069	16.1340	1	0.7799	0.9171	1.7771	0.9018	0.9950	74.7143	48.1659	0.8917

considered equal to 0, because the rock is considered intact, and a new parameter α, as the strength reduction parameter, is considered for extending the generalization of Eq. (5) to anisotropic rocks. The calculated parameters are listed in Table 2.

Furthermore, the coefficient of determination (R^2) is used to evaluate the goodness of fit for each failure criterion. R^2 can be calculated as follows:

$$R^2 = 1 - \frac{\sum_{i=1}^n \left(\sigma_i^t - \sigma_i^p\right)^2}{\sum_{i=1}^n \left(\sigma_i^t - E[\sigma^t]\right)^2}, \tag{7}$$

where σ_i^t and σ_i^p are, respectively, the tested and predicted values of σ for the ith data point, $E[\sigma^t]$ is the expectation of the tested value (in this research, it is considered as the average value), and n is the number of data points. The calculated R^2 values for each criterion are also listed in Table 2.

The failure envelops of different criteria for the shale specimens are plotted in Fig. 11a, b. From Fig. 11a, it can be observed that the linear and non-linear criteria can reflect the relationship of σ_1 versus σ_3 well. From Table 2 and Fig. 12, it is hard to conclude which criterion is better for describing the experiment results, as the R^2 values of the Hoek–Brown criterion are larger than those of the Mohr–Coulomb criterion at certain bedding inclinations (such as 0°, 30°, 60°, 75°), and vice versa at other bedding inclinations. In fact, there is little difference in the R^2 values between the Mohr–Coulomb and Hoek–Brown criteria at bedding inclinations of 15° and 45°. However, the R^2 values of the Hoek–Brown criterion are much larger than those of the Mohr–Coulomb criterion at bedding inclinations of 30°, 60°, and 75°. Therefore, it can be assumed that the Hoek–Brown criterion reflects the
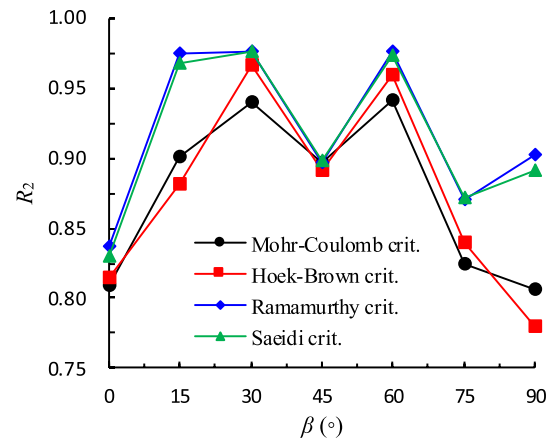

Fig. 12 Comparison of coefficient of determination (R_2) calculated by different strength criterions

experimental results better. Figure 11b illustrates that the Ramamurthy and Saeidi criteria fit the triaxial data well. However, it should be noted that based on Eq. (2), the Ramamurthy criterion cannot predict the failure strength under uniaxial compression, as σ_3 is the denominator and cannot be equal to 0. Therefore, the value predicted by the Ramamurthy criterion shows a significant error when σ_3 is close to 0 MPa. Therefore, when the R^2 values are calculated using the Ramamurthy criterion, the test data obtained under uniaxial compression are not considered. From Table 2 and Fig. 12, it can be seen that the R^2 values of the Ramamurthy and Saeidi criteria are larger than those of the Mohr–Coulomb and Hoek–Brown criteria, which indicates that the two empirical criteria for anisotropic rocks reflect the experiment results better. Although, overall, the Ramamurthy criterion yields
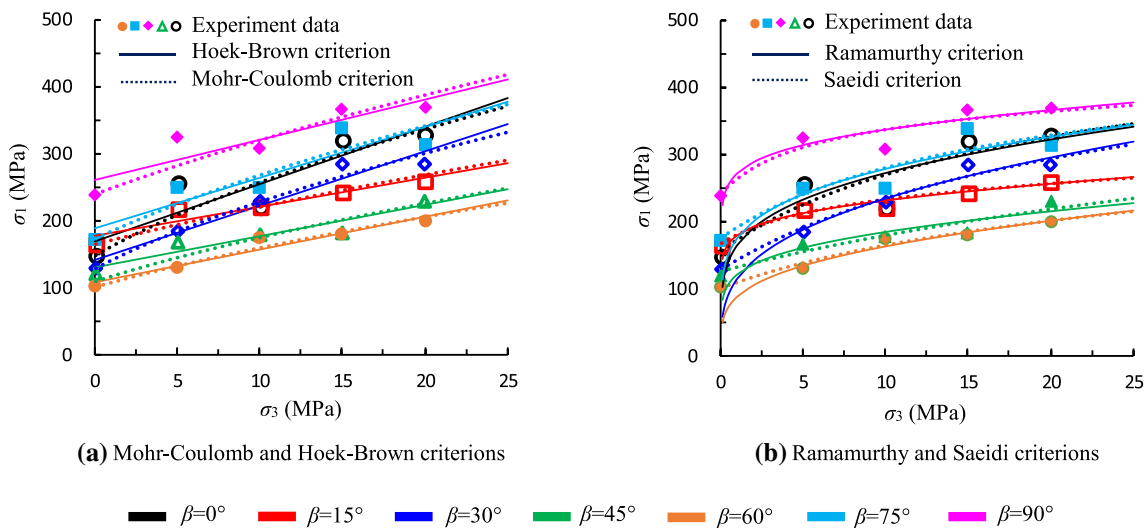

(a) Mohr-Coulomb and Hoek-Brown criterions **(b)** Ramamurthy and Saeidi criterions

Fig. 11 Comparison of failure envelopes of shale specimens at different bedding inclinations

larger R^2 values than those yielded by the Saeidi criterion, it cannot predict UCS and does not work well when σ_3 is close to 0 MPa (e.g., below 5 MPa).

Figure 13 provides a comparison of the strength variation between tested data and the prediction from various criteria. It should be noted that the experimental data of UCS values were used to plot all the curves obtained using the Ramamurthy criterion, as the criterion is unable to predict UCS values because σ_3 is the denominator in Eq. (2) and cannot be equal to 0. Thus, the plotted curve representing the Ramamurthy criterion prediction does not match the data provided in Fig. 11b. From Fig. 13, it can be clearly seen that all the four criteria predict the tested data very well. On the other hand, from the curves of experimental data presented in Fig. 13, it can be seen that, overall, the failure strength displays "U"-type variation with respect to the bedding inclination. The maximum values are observed at $\beta = 90°$ and the minimum values are observed at $\beta = 60°$. It should also be pointed out that at certain bedding inclinations, the tested failure strength values under certain low confining pressures are higher than those under high confining pressures, e.g., the tested value of failure strength under confining pressure 15 MPa is higher than that under confining pressure 20 MPa when $\beta = 75°$. This contradiction indicates the common experimental error caused by the dispersion of specimens. Although the experiment was planned such that the tested specimens under each confining pressure would be prepared from one rock block to reduce dispersion, unfortunately the number of rock blocks was not sufficient to meet this requirement. The individual difference in specimens may impact the tested strength at certain values of β. However, the overall failure strength exhibits an increase in the confining pressure.

4.3 Failure Behavior Analysis

Figure 14 depicts the ultimate failure mode of shale specimens under various confining pressures. All the labels are pasted on the surface, which is orthogonal to the bedding plane (as illustrated in Fig. 5). Therefore, the relative positions of the bedding plane and fracture surface can be presented in a consistent manner. Moreover, owing to the fact that the shale specimens used in this research were highly brittle, all the specimens were banded by Scotch tape before testing to prevent them from breaking into pieces upon failure. Figure 14 indicates that the specimens maintain a good overall shape under the restriction of tape. Furthermore, it should be noted that the specimens were covered by transparent heat-shrink tube to avoid breaking into pieces under uniaxial compression, as the brittle failure under no confined pressure is much stronger than that under confining pressure. As depicted in Fig. 14a, when $\sigma_3 = 0$ MPa, significant damage occurred in the specimens after uniaxial compression, and large circumferential dilatation made it difficult for the tube to be removed. In fact, the Scotch tape still attached to the surface indicates the fracture mode. Furthermore, Fig. 14 indicates that the tapes were dislocated under shear fractures, such as fractures 1#, 2#, and 3#. Therefore, it can be helpful to isolate the shear fracture.

Based on our observations from Fig. 14, the failure behavior of the shale specimens under various confining pressures can be classified into the following modes as illustrated in Fig. 15; Table 3 summarizes the failure modes of shale specimens at various bedding inclinations and under various confining pressures:

1. Tensile splitting through bedding plane (T–T). In this case, as illustrated in Fig. 15a, the tensile crack extends along the axial loading direction and through the bed-
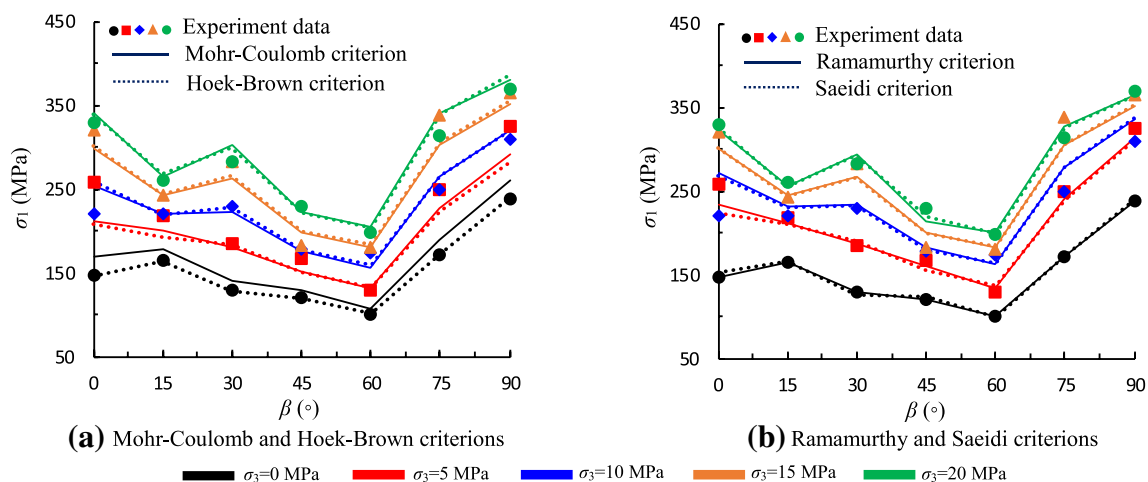

Fig. 13 The strength variation with respect to the bedding inclinations under different confining pressures
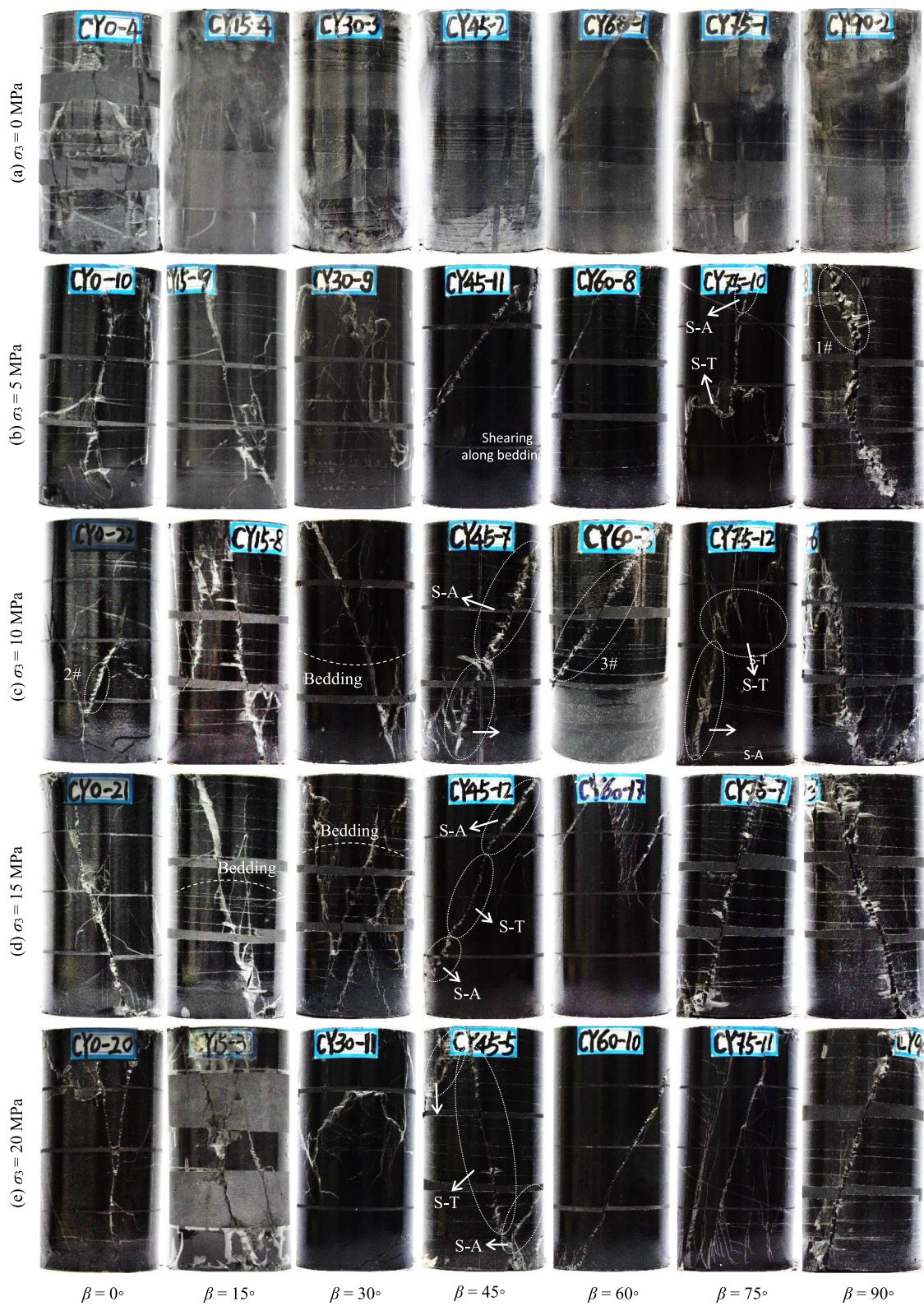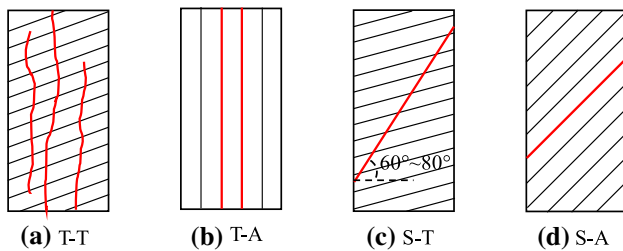
Fig. 14 Ultimate failure mode of shale specimens under different confining pressures

Fig. 15 Ultimate failure mode of shale specimens under different confining pressures

ding planes. This fracture pattern occurs mainly under uniaxial compression. As depicted in Fig. 14a, at $\beta = 0°$, 15°, 30°, 45°, and 75°, the tensile fractures extend from the top to the end through bedding planes, subjecting the specimens to significant dilatation, which indicates high brittleness.

2. Tensile splitting along bedding plane (T–A). This fracture pattern occurs only at $\beta = 90°$. As illustrated in Fig. 15b, in this case, the bedding plane is parallel to the loading direction, and the tensile cracks can easily extend along the bedding planes, as the mechanical properties of the bedding plane are weaker than those of the matrix. Figure 14a indicates that the T–A fractures occur in the specimens at $\beta = 90°$. However, when applied to confining pressure, shear cracks occur instead of T–A cracks.

3. Shear through bedding plane (S–T). This fracture pattern occurs under confining pressure. As illustrated in Fig. 15c, shear fracture extends diagonally along the specimens through the bedding planes. As shown in Fig. 14b–e, the S–T fracture is the most common pattern, and the fracture inclination is approximately 60°–80°. Because of high fracture inclination, it can extend through most bedding planes.

4. Shear along bedding plane (S–A). When the shear fracture inclination is approximately equal to the bedding inclination, S–A fracture occurs. In this case, the number and morphology of fractures is often very simple, in that just one or two straight fractures extend along the bedding plane. Because the mechanical property of the bedding plane is very weak, S–A fracture easily occurs at $\beta = 45°$–75° (as shown in Fig. 14). Therefore, mini-

mum failure strength often occurs at bedding inclinations of 45°–75° (as shown in Fig. 10a).

5 Analysis and Discussion on Brittleness Characteristics

5.1 Discussion on Brittleness Index Based on Rock Mineral Compositions

From a structural point of view, minerals are the fundamental components governing the brittle and ductile behavior of rocks (Kivi et al. 2018). It is generally understood that the presence of brittle mineral content can help promote brittleness in rocks, whereas the presence of ductile minerals diminishes the brittleness. In this paper, the mineral composition of the shale specimens is attained using the XRD test. Brittleness indexes based on rock mineral compositions can be obtained using the formulas of BI_1, BI_2, and BI_3 and are listed in Table 4. In fact, it cannot reach a substantial conclusion by considering only these three brittleness index values, as only one type of shale specimen is tested in this study. For most laboratory investigations, the brittleness index derived from rock mineral compositions is not very helpful unless the research objects are a large number of rock specimens from different sites and formations. Consequently, mineralogy-based indexes are frequently applied to estimate the continuous profiles of brittleness over the entire well in the shale gas development industry. On the other hand, as mentioned in Sect. 3.2, mineralogical brittleness indexes do not consider the significant impact of the stress state on the brittleness of rocks, as it is well established that a rock tends to exhibit lower brittleness under elevated confining stresses. Moreover, diagenetic processes also have a distinct impact on brittleness characteristics. The brittleness of rocks with the same mineral assembly but different porosities, densities, and textures may also differ substantially because of being subject to distinct physical, chemical, or biological

Table 4 Results of BI_1, BI_2 and BI_3

Brittleness index	BI_1	BI_2	BI_3
Value	0.465	0.639	0.846

Table 3 Failure mode summary of shale specimens in this research

	$\beta=0°$	$\beta=15°$	$\beta=30°$	$\beta=45°$	$\beta=60°$	$\beta=75°$	$\beta=90°$
$\sigma_3=0$ MPa	T–T	T–T	T–T	T–T	S–A	T–T	T–A
$\sigma_3=5$ MPa	S–T	S–T	S–T	S–A	S–A	S–A, S–T	S–T
$\sigma_3=10$ MPa	S–T	S–T	S–T	S–A, S–T	S–A	S–A, S–T	S–T
$\sigma_3=15$ MPa	S–T	S–T	S–T	S–A, S–T	S–A	S–A	S–T
$\sigma_3=20$ MPa	S–T	S–T	S–T	S–A, S–T	S–A	S–A	S–T

diagenetic processes. This implies that mineralogical compositions cannot solely be applied to accurately estimate the brittleness of rocks and it is critical to consider other rock fabric properties and environmental conditions (Kivi et al. 2018).

5.2 Analysis and Discussion on Brittleness Index Based on Stress–Strain Curve and Energy Balance

Brittleness indexes based on the stress–strain curve and energy balance are commonly used in laboratory investigations, as the stress–strain curve can easily be obtained by conducting the triaxial compression test and, most significantly, it reflects the brittleness response to the stress state.

BI_{10} indicates the degree of brittleness by characterizing the loss of strength of the rock material. The brittle failure of rock is often accompanied by a strong release of energy. Thus, the specimen is significantly damaged, and its strength reduces remarkably, leading to a very low level of the stress–strain curve. Higher the BI_{10} value, higher is the brittleness. When $BI_{10} = 1$, the rock completely loses its bearing capacity, indicating that the brittleness is very high. When the value is equal to 0, the rock displays ideal plasticity and its strength does not reduce, which indicates very high ductility. However, the amplitude of strength loss only reflects the degree of failure of the specimen but cannot reflect the rate of the failure process, which is also a key manifestation of brittleness. As depicted in Fig. 16, it is assumed that the five stress–strain curves (P_1, P_2, P_3, P_4, P_5) depict the same failure strength and residual strength. According to BI_{10}, these five specimens have the same brittleness magnitude. However, from their curve shapes, it can be concluded that they have different brittleness behaviors. The P_1 and P_3 curves have no plastic strain. However, the stress of P_1 drops much faster than that of P_2, indicating that P_1 has higher brittleness; the P_2, P_4, and P_5 curves have the same peak plastic strains.
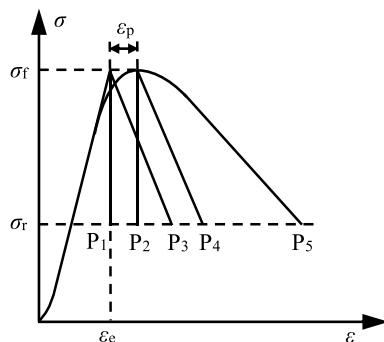
However, their stresses reduce at different rates, indicating that they have different degrees of brittleness. From this discussion, it can be concluded that both the degree and rate of decrease in strength are key factors that must be applied to evaluate the brittleness of rocks. Therefore, a brittleness index that considers both the degree and rate of decrease in strength is necessary. The new brittleness index BI^*_1 proposed in this study is expressed as

$$BI^*_1 = \frac{\sigma_f - \sigma_r}{\sigma_f} \lg |M|, \tag{8}$$

where σ_f and σ_r are the failure strength and residual strength, respectively, characterizing the degree of strength loss, and M is the post-peak modulus, characterizing the rate of strength loss.

BI_{11} characterizes the degree of elastic deformation before the peak. It can be easily understood that higher brittleness leads to higher resilience, which is caused by a larger elastic proportion. Similarly, if the energy aspects at failure are considered, BI_{11} can be transformed into a form of energy, which is expressed by Eq. (9), characterized as a ratio of elastic energy (U_{et}) to ideal elastic energy (U_{ei}) at failure:

$$BI_{11} = \frac{\varepsilon_e}{\varepsilon_t} = \frac{\varepsilon_e \sigma_f / 2}{\varepsilon_t \sigma_f / 2} = \frac{U_{et}}{U_{ei}}, \tag{9}$$

where the ideal elastic energy (U_{ei}) is a new energy parameter defined in this research, which is not a real energy stored in rocks. Instead, as shown in Fig. 17, it is defined and characterized as the area of the triangle formed by the point o, the peak point, and the projection of the peak on the x-coordinate. From another point of view, it can be regarded as the elastic energy of an ideal elastic stress–strain curve with a secant modulus of the peak to the original point. Similarly, BI_{13} is characterized as a ratio of the elastic energy (U_{et}) to the absorbed energy ($U_{et} + U_p$) at failure:

$$BI_{13} = U_{et} / (U_{et} + U_p). \tag{10}$$

The absorbed energy is divided into two parts, one is stored in rock as elastic energy and another part is dissipated because of plastic deformation. It can be characterized as the area under the stress–strain curve before the peak and calculated using the integral of stress–strain curve before the peak. Figure 17 indicates that for brittle failure, little plastic deformation occurs before the peak, and the absorbed energy ($U_{et} + U_p$) is less than the ideal elastic energy (U_{ei}). With an increase in the plastic deformation, the absorbed energy ($U_{et} + U_p$) turns out to be larger than the ideal elastic energy (U_{ei}), and the brittleness tends to be lower. Therefore, another new brittleness
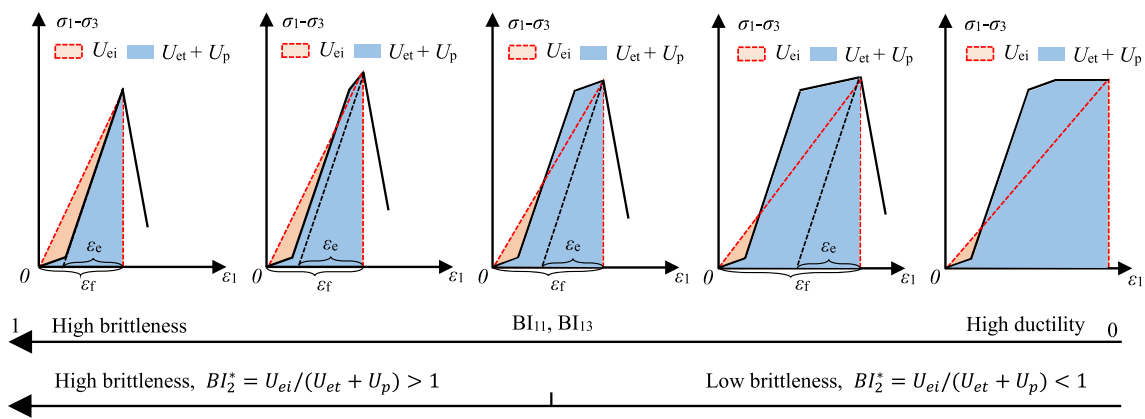

Fig. 16 Stress–strain curves show different brittleness degree, but are of equal peak and residual strength levels

Fig. 17 Scales of the BI_{11}, BI_{13} and BI^*_2 with characteristic stress–strain curves before peak

index, BI^*_2, can be defined as a ratio of the ideal elastic energy (U_{ei}) to the absorbed energy ($U_{et} + U_p$) at failure. As shown in the following equation, its magnitude is also equal to the ratio of BI_{13} to BI_{11}:

$$BI^*_2 = U_{ei}/(U_{et} + U_p) = BI_{13}/BI_{11}. \tag{11}$$

As shown in Fig. 17, the same as BI_{11} and BI_{13}, BI^*_2 can reflect the brittleness very well. With rock material becoming more brittle, BI_{11}, BI_{13}, and BI^*_2 tend to be higher. The values of BI_{11} and BI_{13} approach 1 when the rock material becomes very highly brittle, and the value of BI^*_2 is larger than 1 when the rock material is highly brittle. Although BI_{11}, BI_{13}, and BI^*_2 can reflect the brittleness well, they do not account for the post-peak characteristics of brittle rock. In fact, the post-peak characteristics of the stress–stain curve are also key to understanding the brittleness of rocks. Highly brittle rock material mostly fails when the stress drops steeply to a very low level. Therefore, the brittleness index calculated considering the characteristics of the whole stress–stain curve is more effective.

As defined in Table 1 and illustrated in Fig. 7, the indexes BI_{14}, BI_{15}, BI_{16}, BI_{17}, BI_{18}, BI_{19}, and BI_{20} are calculated by considering the energy evolution during the entire rock failure process. Figure 18 illustrates how these brittleness indexes reflect brittle characteristics. When the rock material is undergoing Class II failure (self-sustaining), it exhibits high brittleness, and the additional energy (U_a) is calculated to be negative. Thus, for such cases, the brittleness indexes BI_{15} and BI_{20} can be negative. Figure 18 indicates that with an increase in the brittleness, the magnitudes of BI_{14}, BI_{15}, BI_{19}, and BI_{20} tend to be lower. On the contrary, the magnitudes of BI_{16}, BI_{17}, and BI_{18} turn out to be higher. This can easily be understood based on the illustration from Fig. 7: the dominant variable is the additional energy, which is the numerator in BI_{14}, BI_{15}, BI_{19}, and BI_{20}; however, the additional energy is the denominator in BI_{16}, BI_{17}, and BI_{18}. For highly brittle rock material, the additional energy is very less. Thus, the magnitudes of BI_{14}, BI_{15}, BI_{19}, and BI_{20} are small and those of BI_{16}, BI_{17}, and BI_{18} are large.

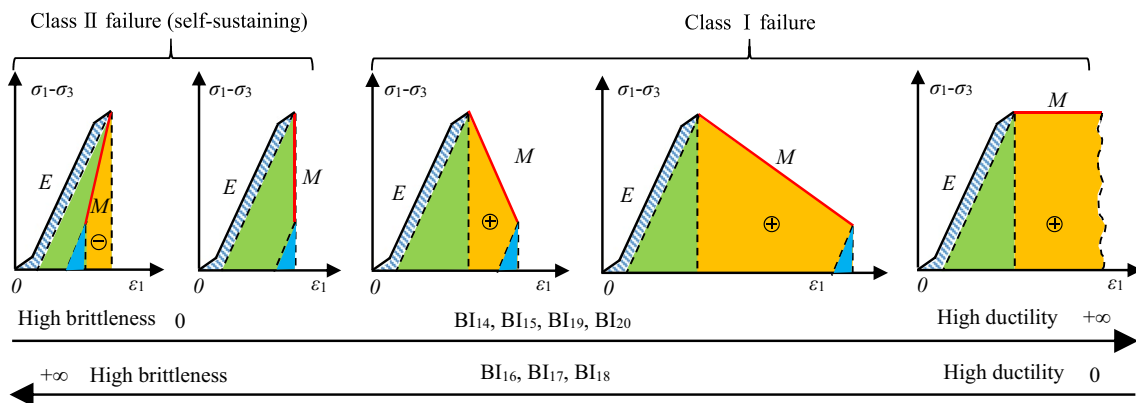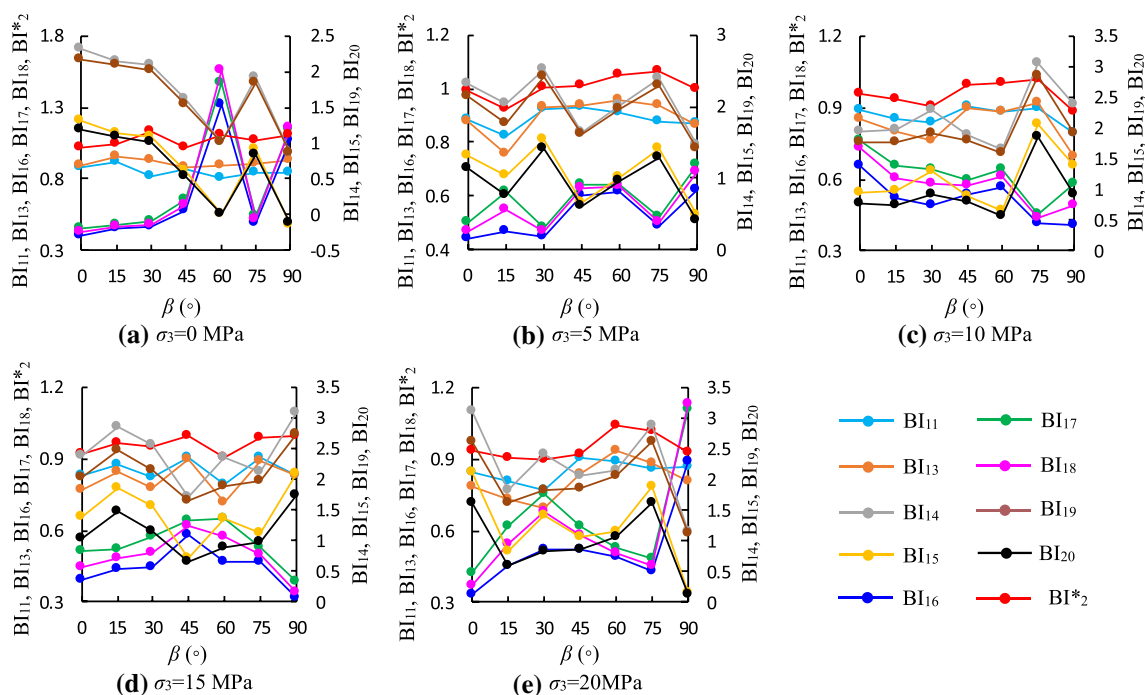Figure 19 illustrates the impact of bedding inclination on the brittleness index under various confining pressures.

Fig. 18 Scales of the BI_{14}–BI_{20} with characteristic stress–strain curves

Fig. 19 Brittleness index variation with respect to bedding inclinations under different confining pressures

The figure indicates that the bedding inclination has a distinct impact on the brittleness index. However, the variation is not uniform under different confining pressures. Under uniaxial compression (Fig. 19a), BI_{11} and BI_{13}, which only consider the impact of pre-peak plastic strain states, seem to have no distinct changes with rising bedding inclination. However, $BI*_2$, which is defined based on BI_{11} and BI_{13}, roughly increases gradually with rising bedding inclination. BI_{14}, BI_{15}, BI_{16}, BI_{17}, BI_{18}, BI_{19}, and BI_{20}, which consider the impact of post-peak stress drop, also indicate that the brittleness roughly increases with rising bedding inclination, although the brittleness at $\beta = 75°$ decreases to a low level. It indicates that the new brittleness index $BI*_2$ proposed in this research can reflect the brittleness well. When $\sigma_3 = 5$ MPa (Fig. 19b), BI_{11}, BI_{13}, and $BI*_2$ indicate that the brittleness roughly increases gradually with rising bedding inclination, whereas BI_{14}, BI_{15}, BI_{16}, BI_{17}, BI_{18}, BI_{19}, and BI_{20} show undulatory variation. For other confining pressures ($\sigma_3 = 10$, 15 and 20 MPa), BI_{11}, BI_{13}, and $BI*_2$ exhibit an overall increase before $\beta = 60°$–$75°$ and then decrease. However, BI_{14}, BI_{15}, BI_{16}, BI_{17}, BI_{18}, BI_{19}, and BI_{20} demonstrate different variations. BI_{16}, BI_{17}, and BI_{18} decrease with rising bedding inclination under $\sigma_3 = 10$ MPa and demonstrate undulatory variation at $\sigma_3 = 15$ and 20 MPa. BI_{14}, BI_{15}, BI_{19}, and BI_{20} indicate more undulant variation with rising bedding inclination at $\sigma_3 = 10$, 15, and 20 MPa. This indicates that a brittleness index that considers the impact of pre-peak plastic strain states demonstrates a different applicability compared to a brittleness index that considers the stress–strain characteristic and energy evolution during the entire process.

Figure 20 presents the confining pressure effect on the brittleness index under different bedding inclinations. From Fig. 20, it can be observed that BI_{11}, BI_{13}, and $BI*_2$ indicate that the overall brittleness decreases with an increase in the confining pressure, which corresponds to the results of Kivi's research (Kivi et al. 2018). However, BI_{14}, BI_{15}, BI_{16}, BI_{17}, BI_{18}, BI_{19}, and BI_{20} do not demonstrate a distinct decrease with rising confining pressure and generally do not represent the relative brittleness sequences in a suitable manner. In particular, some cases reflect reverse brittleness variation with rising confining pressure. For example, BI_{16}, BI_{17}, and BI_{18} indicate a rough increase with rising confining pressure when $\beta = 30°$. BI_{14}, BI_{15}, BI_{19}, and BI_{20} indicate undulant variation with rising confining pressure although an overall increase in the variation of brittleness. This type of irregular variation is also reflected by Kivi's research (Kivi et al. 2018). In Kivi's research, BI_{19} and BI_{20} also indicate undulant variation in brittleness with rising confining pressure and represent neither a meaningful evolution pattern with confining pressure nor a recognizable relative brittleness sequence. It thus appears that the reviewed energy-based brittleness indexes (BI_{14}, BI_{15}, BI_{16}, BI_{17}, BI_{18}, BI_{19}, and BI_{20}) cannot fully reflect the brittleness characteristics of rock material. After comprehensively interpreting the
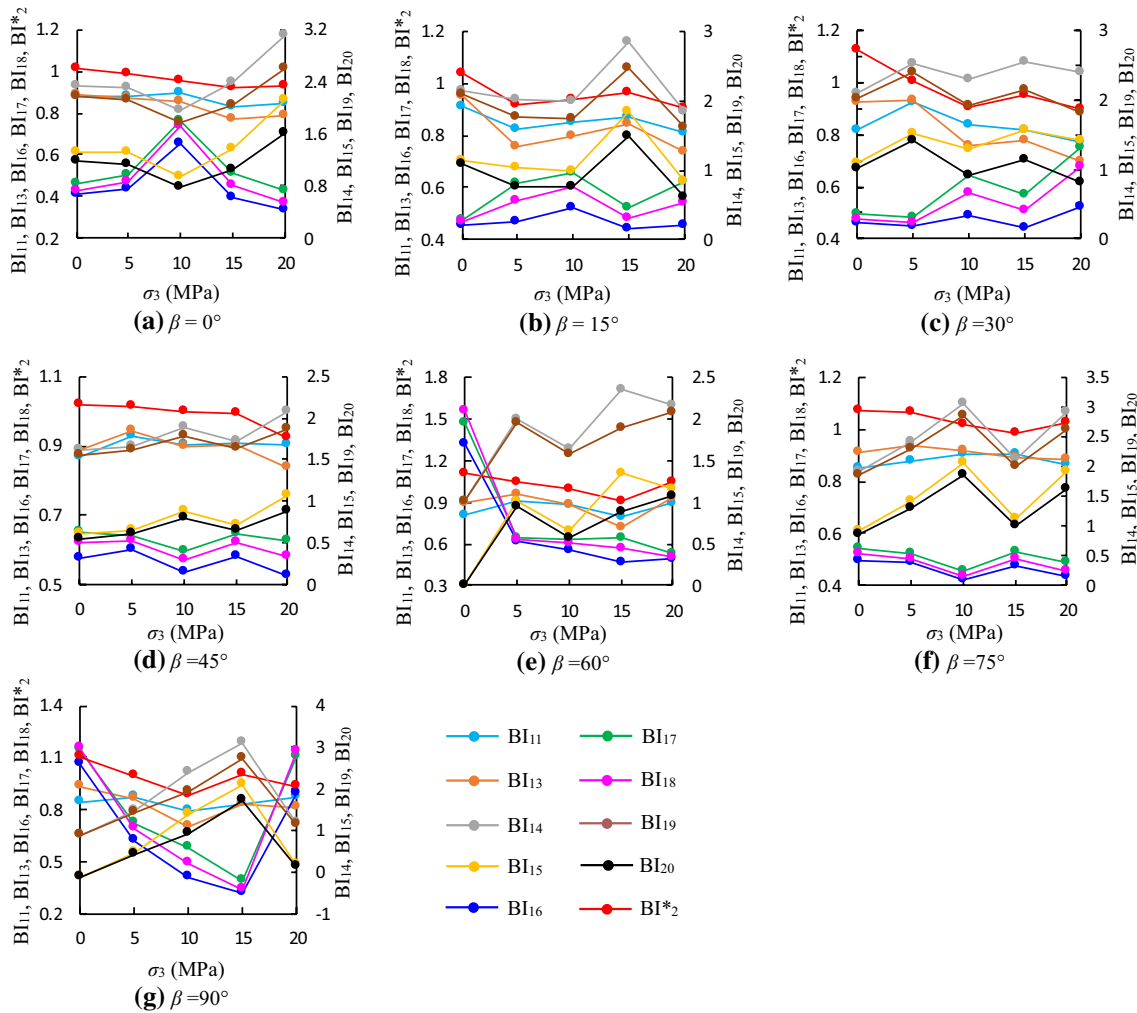
Fig. 20 Brittleness index variation with respect to confining pressures at different bedding inclinations

complete stress–strain curves on the basis of energy transformations, Kivi et al. (2018) established a new index, referred to herein as BI_{21}, to precisely quantify the main characteristics of brittle failure. In this framework, BI_{21} is defined as follows:

$$BI_{21} = 0.5\left(BI_{new\text{-}I} + BI_{new\text{-}II}\right) = 0.5(U_{ec}/U_r + U_{ec}/(U_{et} + U_p)),$$
(11)

where $BI_{new\text{-}I}$ determines the extent to which the fracturing process occurs in a self-sustaining manner (Class II failure illustrated in Fig. 18) and $BI_{new\text{-}II}$ represents the fraction of the total absorbed energy in the pre-peak stage that is consumed during the post-peak rupture process. Consequently, BI_{21} not only treats the entire process of failure but also describes the entire range of Class I rock failure behavior (Class I failure illustrated in Fig. 18), from absolute ductility to absolute brittleness, in a continuous scale corresponding to 0–1. Therefore, it is expected that the relationships established between the pre- and post-peak characteristics

in BI_{21} formulation provide a more appropriate measure of the brittleness of rocks.

5.3 Comparison of BI*$_1$ and BI*$_2$ with BI$_{21}$

In this research, two new brittleness indexes $BI*_1$ and $BI*_2$ are proposed. $BI*_1$ synthesizes the peak stress drop magnitude and rate. Essentially, $BI*_2$ is considered to qualitatively distinguish the brittleness grades by characterizing the plastic deformation before the peak, same as BI_{11} and BI_{13}. BI_{21} synthesizes the pre- and post-peak characteristics. Figure 21 illustrates the variations in $BI*_1$, $BI*_2$, and BI_{21} with increases in bedding inclination, and Fig. 22 plots the $BI*_1$, $BI*_{22}$, and BI_{21} variations with increases in confining pressure.

Figure 21 clearly indicates that although the value ranges are much different, $BI*_1$ and BI_{21} demonstrate very similar variation, roughly increasing gradually with an increase in the bedding inclination. However, $BI*_2$ demonstrates a
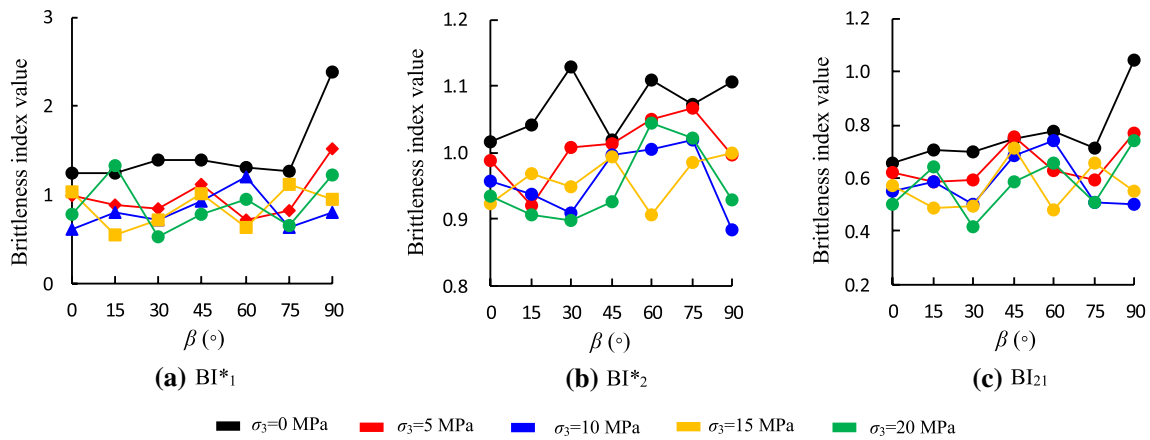
Fig. 21 $BI*_1$, $BI*_2$ and BI_{21} variation with respect to bedding inclinations under different confining pressures
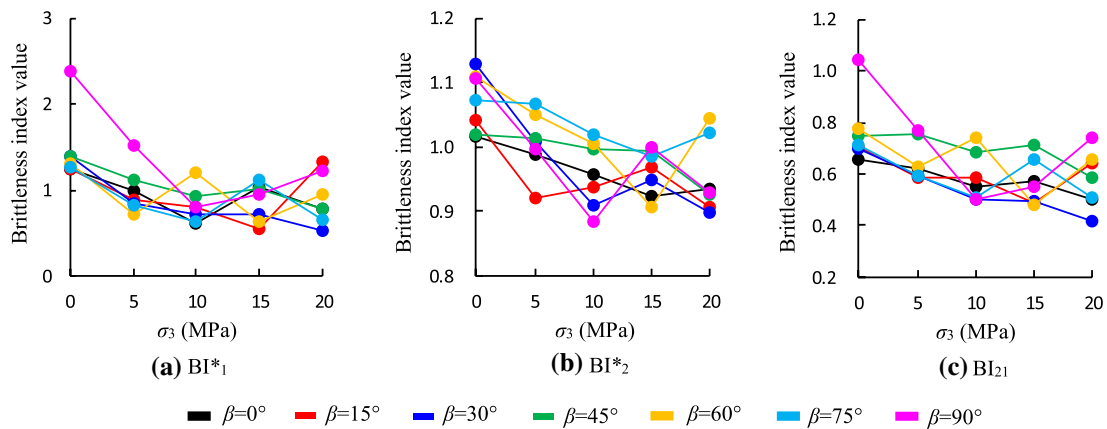

Fig. 22 $BI*_1$, $BI*_2$ and BI_{21} variation with respect to confining pressures at different bedding inclinations

much different type of variation. Figure 22 indicates that $BI*_2$ displays a more complex type of variation, and no clear relationship is observed to be dominant between $BI*_2$ and the bedding inclination. On the other hand, Fig. 22 also indicates that $BI*_1$ and BI_{21} show a similar brittleness variation, roughly decreasing gradually with increase in the bedding inclination, and that particularly under uniaxial compression, the specimens at $\beta = 90°$ have a much higher brittleness value than those at any other bedding inclination. Although $BI*_2$ also demonstrates a decreasing variation with an increase in the bedding inclination, the entire trend is a bit different from those of $BI*_1$ and BI_{21}. To summarize, the confining pressure contributes to the transition from brittleness to ductility of rock material. However, compared to $BI*_2$, $BI*_1$ and BI_{21} show more validity and accuracy on the brittleness evaluation criterion for this shale specimen. This evidently reveals that multiple stress–strain characteristics should be taken into account for the evaluation of the brittleness of rocks. An index that only characterizes a single

factor of stress–strain characteristics or energy evolution cannot definitely be representative of specific brittleness.

5.4 Discussion on Relationship Between Brittle Characteristics and Failure Mode

According to the discussion in the preceding section, although the bedding inclination has a distinct impact on the brittle characteristics of shale specimens, it shows no particular sequential variation. When considering the relationship between the brittle characteristics and failure mode, some connections can be found. As stated in Sect. 3.2, the release of elastic energy leads to crack propagation and macro fractures in specimens, and high brittleness leads to a strong release of elastic energy, which is reflected by the fracture pattern after failure. In Sect. 4.3, it was stated that a specimen is mainly undergoing tensile splitting failure when it is under uniaxial compression, and tensile splitting through the bedding plane (T–T) occurs at $\beta = 0°$–$75°$ and

tensile splitting along the bedding plane (T–A) occurs at $\beta = 90°$. When subjected to confining pressure, it changes to shear fracture, including shearing through the bedding plane (S–T) occurring at $\beta = 0°$–30° and 90° and shearing along the bedding plane (S–A) occurring at $\beta = 45°$–75°.

From Figs. 21 and 22, it can be found that brittleness under uniaxial compression is higher than that under confining pressure, and the former leads to tensile splitting failure. It reveals that the brittleness of specimens during tensile splitting failure is higher than that during shear failure. It can be easily understood that shearing leads to slipping along the fracture plane, which leads to further plastic deformation and energy dissipation and lower brittleness as a consequence. This is the impact of confining pressure on brittleness. In particular, specimens at $\beta = 90°$ under uniaxial compression, which are in the T–A failure mode, show the highest brittleness compared to specimens at other bedding inclinations, which are in the T–T failure mode. This indicates that the T–A failure mode leads to higher brittleness than the T–T failure mode. It can be explained that the bedding plane is weaker than the matrix. Thus, once damage occurs in the bedding plane, fractures extend at high speed along it, and the stored elastic energies are released rapidly, which lead to low plastic deformation and a sharp drop in stress. On the other hand, Fig. 21 indicates that under confining pressure, specimens at $\beta = 45°$–75°, which are in the S–A failure mode, show higher brittleness than those at other bedding inclinations, which are in the S–T failure mode, particularly based on the indication of BI_{21}. This can be attributed to the fact that a weak bedding plane cannot provide enough plastic deformation and energy dissipation, and, as a consequence, shear fracture extends more easily along the bedding plane than through it. Therefore, the overall relationship between brittleness and failure mode can be concluded as follows: T–A > T–T > S–A > S–T.

6 Conclusions

In this research, shale specimens collected from an outcrop of the lower Silurian Longmaxi formation at the Sichuan Basin of southwestern China were investigated under conventional triaxial compression. The anisotropic behavior of shale specimens under conventional triaxial compression, including the strength, deformation, and failure behaviors, was analyzed. Furthermore, the brittleness characteristics of the shale specimens were analyzed at various bedding inclinations under various confining pressures. Various brittleness indexes, including the new one proposed in this research, were used to evaluate the brittleness of shale. The anisotropy and confining pressure effect on brittleness were discussed in detail.

The linear Mohr–Coulomb, Hoek–Brown, and other failure criteria of anisotropic rocks such as Ramamurthy's and Saeidi's, were used to describe the failure strength in this research. The results indicate that two of the four criteria predict the tested data very well. However, Ramamurthy's and Saeidi's empirical criteria for anisotropic rocks reflected the experiment results better than the linear Mohr–Coulomb and Hoek–Brown criteria. Although, overall, the Ramamurthy criterion showed larger R^2 values than those of the Saeidi criterion, it could not predict UCS and did not work well when σ_3 was close to 0 MPa. After failure, the stress–strain curves and fracture patterns indicated that the shale specimens are highly brittle; in particular, under uniaxial compression, the specimens failed into pieces under tensile splitting. Four failure modes of shale specimens at different bedding inclinations and under different confining pressures can be summarized—tensile splitting through the bedding plane (T–T), tensile splitting along the bedding plane (T–A), shear through the bedding plane (S–T), and shear along the bedding plane (S–A). When confining pressures were applied, the specimens failed by shear fracture. The shear along the bedding plane mainly occurred at $\beta = 45°$–75°, and at other bedding inclinations, shear fracture extends through bedding planes by a fracture inclination of approximately 60°–80°. Based on the anisotropy and confining pressure effects on brittleness, which are reflected by $BI*_1$, $BI*_2$, and BI_{21}, the relationship between brittleness and failure mode was revealed. The fractures that extend along bedding plane demonstrate higher brittleness than those that extend through bedding plane. Thus, the weaker bedding plane provided lower plastic deformation and energy dissipation than the rock matrix. As a consequence, the order of brittleness was concluded as follows: T–A > T–T > S–A > S–T.

At present, several brittleness indexes have been defined to evaluate the brittle characteristics of rock material. The mineralogical brittleness indexes do not consider the significant impact of the stress state on the brittleness of rocks, as it is well established that a rock tends to show lower brittleness under elevated confining stresses. In general, brittleness indexes only consider the impact of pre-peak plastic strain states and are, thus, not comprehensive because certain rock materials exhibit a distinct transformation from brittleness to ductility after the peak under high confining pressures, although they show no large plastic deformation before the peak. However, under low confining pressures or when the rock material has high intrinsic brittleness, the specimens show strong brittleness, and the stress drops sharply to a low level after the peak. In this case, the stress–strain characteristics and energy evolution in different specimens are similar, and these no longer play a particularly significant role in the estimation of brittleness. Therefore, brittleness indexes that consider only the impact of pre-peak plastic strain states are appropriate; these can reflect the brittleness as well. To

further improve the framework of brittleness evaluation, new brittleness indexes BI^*_1 characterizing the peak stress drop magnitude and rate, and BI^*_2, based on the energy evolution pre-peak, were proposed in this study. By comparing BI^*_1 and BI^*_2 to other indexes, it was concluded that BI^*_1 provides good validity and accuracy in terms of the brittleness evaluation criterion, same as another comprehensive index BI_{21} does. Although BI^*_2 demonstrates good efficiency, it is a bit different from BI^*_1. It should be understood that the reliability of a highly effective brittleness index in practice depends on the captured formulation strategy in accounting for various rock pre-peak and post-peak performance and failure characteristics. To unquestionably validate the performance of the indexes, further experimental tests and analysis of various types of rock materials are necessary.

Compliance with Ethical Standards

Conflict of interest The authors declare no conflict of interests.

References

Ai C, Zhang J, Li YW, Zeng J, Yang XL, Wang JG (2016) Estimation criteria for rock brittleness based on energy analysis during the rupturing process. Rock Mech Rock Eng 49:4681–5698

Altindag R (2002) The evaluation of rock brittleness concept on rotary blast hole drills. J S Afr Inst Min Metall 102(1):61–66

Andreev GE (1995) Brittle failure of rock materials: test results and constitutive models. A.A. Balkema, Rotterdam, p 446

Bishop AW (1967) Progressive failure with special reference to the mechanism causing it. In: Proceedings of the geotechnical conference, Oslo, pp 142–150

Chen L, Shao JF, Huang HW (2010) Coupled elastoplastic damage modeling of anisotropic rocks. Comput Geotech 37(1–2):187–194

Chen L, Shao JF, Zhu QZ, Duveau G (2012) Induced anisotropic damage and plasticity in initially anisotropic sedimentary rocks. Int J Rock Mech Min Sci 51:13–23

Chen Y, Jin Y, Chen M, Yi Z, Zheng X (2017) Quantitative evaluation of rock brittleness based on the energy dissipation principle, an application to type II mode crack. J Nat Gas Sci Eng 45:527–536

Cho JW, Kim H, Jeon S, Min KB (2012) Deformation and strength anisotropy of Asan gneiss, Boryeong shale, and Yeoncheon schist. Int J Rock Mech Min Sci 50:158–169

Fairhurst CE, Hudson JA (1999) Draft ISRM suggested method for the complete stress–strain curve for intact rock in uniaxial compression. Int J Rock Mech Min Sci 36(3):279–289

Hajiabdolmajid V, Kaiser P, Martin C (2003) Mobilised strength components in brittle failure of rock. Géotechnique 53(3):327–336

Hakala M, Kuula H, Hudson JA (2007) Estimating the transversely isotropic elastic intact rock properties for in situ stress measurement data reduction: a case study of the Olkiluoto mica gneiss, Finland. Int J Rock Mech Min Sci 44:14–46

Heap MJ, Baud P, Meredith PG (2009) Influence of temperature on brittle creep in sandstones. Geophys Res Lett 36:L19305. https://doi.org/10.1029/2009GL039373

Heng S, Guo Y, Yang C, Daemen JJK, Li Z (2015) Experimental and theoretical study of the anisotropic properties of shale. Int J Rock Mech Min Sci 74(1):58–68

Hetényi M (1950) Hand book of experimental stress analysis. Wiley, New York

Hoek E, Brown ET (1980) Underground excavations in rock. Institution of Mining and Metallurgy, London

Hoek E, Brown ET (1997) Practical estimates of rock mass strength. Int J Rock Mech Min Sci 34(8):1165–1186

Holt RM, Fjaer E, Nes OM, Alassi HT (2011) A shaly look at brittleness. In: 45th US rock mechanics/geomechanics symposium. American Rock Mechanics Association, vol 11–366

Howell JV (1960) Glossary of geology and related sciences. American Geological Institute, Washington, DC

Hucka V, Das B (1974) Brittleness determination of rocks by different methods. Int J Rock Mech Min Sci Geomech Abstr 17(10):389–392

ISRM (2007) The complete ISRM suggested methods for rock characterization, testing and monitoring: 1974–2006. In: Ulusay R, Hudson JA (eds) Prepared by the commission on testing methods. ISRM, Ankara

Jaeger JC (1960) Shear failure of transversely isotropic rock. Geol Mag 97:65–72

Jarvie DM, Hill RJ, Ruble TE, Pollastro RM (2007) Unconventional shale-gas systems: the Mississippian Barnett shale of north-central Texas as one model for thermogenic shale-gas assessment. AAPG Bull 91(4):475–499

Jin X, Shah SN, Roegiers JC, Zhang B (2014a) Fracability evaluation in shale reservoirs-an integrated petrophysics and geomechanics approach. In: Proceedings of the SPE hydraulic fracturing technology conference, Society of Petroleum Engineers

Jin X, Shah SN, Truax JA, Roegiers J-C (2014b) A Practical petrophysical approach for brittleness prediction from porosity and sonic logging in shale reservoirs. In: SPE annual technical conference and exhibition, Society of Petroleum Engineers

Jin X, Shah SN, Roegiers JC, Zhang B (2015) An integrated petrophysics and geomechanics approach for fracability evaluation in shale reservoirs. Soc Pet Eng J 20(3):518–526

Josh M, Esteban L, Piane CD, Sarout J, Dewhurst DN, Clennell MB (2012) Laboratory characterisation of shale properties. J Pet Sci Eng 88–89(2):107–124

Kim H, Cho JW, Song I, Min KB (2012) Anisotropy of elastic moduli, p-wave velocities, and thermal conductivities of Asan gneiss, Boryeong shale, and Yeoncheon schist in Korea. Eng Geol 147–148(5):68–77

Kivi IR, Ameri M, Molladavoodi H (2018) Shale brittleness evaluation based on energy balance analysis of stress–strain curves. J Pet Sci Eng 167:1–19

Kuila U, Dewhurst DN, Siggins AF, Raven MD (2011) Stress anisotropy and velocity anisotropy in low porosity shale. Tectonophysics 503(1–2):34–44

Li X, Lei X, Li Q, Li X (2017) Experimental investigation of sinian shale rock under triaxial stress monitored by ultrasonic transmission and acoustic emission. J Nat Gas Sci Eng 43:110–123

Masri M, Sibai M, Shao JF, Mainguy M (2014) Experimental investigation of the effect of temperature on the mechanical behavior of Tournemire shale. Int J Rock Mech Min Sci 70(9):185–191

Morley A (1944) Strength of materials: with 260 diagrams and numerous examples. Longmans, Green and Company, New York

Munoz H, Taheri A, Chanda EK (2016) Fracture energy-based brittleness index development and brittleness quantification by pre-peak strength parameters in rock uniaxial compression. Rock Mech Rock Eng 49:4587–4606

Nasseri MH, Rao KS, Ramamurthy T (1997) Failure mechanism in schistose rocks. Int J Rock Mech Min Sci 34(3–4):219

Nasseri MH, Rao KS, Ramamurthy T (2003) Anisotropic strength and deformational behavior of Himalayan schists. Int J Rock Mech Min Sci 40:3–23

Niandou H, Shao JF, Henry JP, Fourmaintraux D (1997) Laboratory investigation of the mechanical behavior of Tournemire shale. Int J Rock Mech Min Sci 34(1):3–16

Nygård R, Gutierrez M, Bratli RK, Høeg K (2006) Brittle–ductile transition, shear failure and leakage in shales and mudrocks. Mar Pet Geol 23(2):201–212

Obert L, Duvall WI (1967) Rock mechanics and the design of structures in rock (No. Book). Wiley, Hoboken

Qi M, Giraud A, Colliat JB, Shao JF (2016a) A numerical damage model for initially anisotropic materials. Int J Solids Struct 100–101:245–256

Qi M, Shao JF, Giraud A, Zhu QZ, Colliat JB (2016b) Damage and plastic friction in initially anisotropic quasi brittle materials. Int J Plast 82:260–282

Rafiai H (2011) New empirical polyaxial criterion for rock strength. Int J Rock Mech Min Sci 48(6):922–931

Ramamurthy T (1993) Strength, modulus responses of anisotropic rocks. In: Hudson JA (ed) Compressive rock engineering, vol 1. Pergamon, Oxford, pp 313–329

Ramamurthy T, Rao GV, Singh J (1988) A strength criterion for anisotropic rocks. In: Proceedings of the fifth Australia–New Zealand conference on geomechanics, vol 1. Sydney, pp 253–257

Ramsey J (1968) Folding and fracturing of rock. McGraw-Hill, New York

Rao KS, Rao GV, Ramamurthy T (1986) A strength criterion for anisotropic rocks. Ind Geotech J 16(4):317–333

Rickman R, Mullen MJ, Petre JE, Grieser WV, Kundert D (2008) A practical use of shale petrophysics for stimulation design optimization: all shale plays are not clones of the Barnett Shale. In: Proceedings of the SPE annual technical conference and exhibition, Society of Petroleum Engineers

Rybacki E, Reinicke A, Meier T, Makasi M, Dresen G (2015) What controls the mechanical properties of shale rocks?—part I: strength and young's modulus. J Pet Sci Eng 135:702–722

Saeidi O, Vaneghi RG, Rasouli V, Gholami R (2013) A modified empirical criterion for strength of transversely anisotropic rocks with metamorphic origin. Bull Eng Geol Environ 72(2):257–269

Saeidi O, Vaneghi RG, Rasouli V, Gholami R, Torabi SR (2014) A modified failure criterion for transversely isotropic rocks. Geosci Front 5:215–225

Shi XC, Yang X, Meng XF (2016) An anisotropic strength model for layered rocks considering planes of weakness. Rock Mechd Rock Eng 49:3783–3792

Singh M, Samadhiya NK, Kumar A (2015) A nonlinear criterion for triaxial strength of inherently anisotropic rocks. Rock Mech Rock Eng 48:1387–1405

Tarasov B, Potvin Y (2013) Universal criteria for rock brittleness estimation under triaxial compression. Int J Rock Mech Min Sci 59:57–69

Tien YM, Kuo MC (2001) A failure criterion for transversely isotropic rocks. Int J Rock Mech Min Sci 38:399–412

Wong TF, David C, Zhu W (1997) The transition from brittle faulting to cataclastic flow in porous sandstones: mechanical deformation. J Geophys Res Solid Earth 102(B2):3009–3025

Wu S, Ge H, Wang X, Meng F (2017) Shale failure processes and spatial distribution of fractures obtained by ae monitoring. J Nat Gas Sci Eng 41:82–92

Yagiz S (2009) Assessment of brittleness using rock strength and density with punch penetration test. Tunn Undergr Space Technol 24(1):66–74

Yang SQ, Ranjith PG, Huang YH, Yin PF, Jing HW, Gui YL, Yu QL (2015) Experimental investigation on mechanical damage characteristics of sandstone under triaxial cyclic loading. Geophys J Int 201(2):662–682

Yang SQ, Ranjith PG, Jing HW, Tian WL, Ju Y (2017) An experimental investigation on thermal damage and failure mechanical behavior of granite after exposure to different high temperature treatments. Geothermics 65:180–197

Yang SQ, Yin PF, Huang YH (2019) Experiment and discrete element modelling on strength, deformation and failure behaviour of shale under Brazilian compression. Rock Mech Rock Eng 52(11):4339–4359

Yao C, Jiang QH, Shao JF, Zhou CB (2016) A discrete approach for modeling damage and failure in anisotropic cohesive brittle materials. Eng Fract Mech 155:102–118

Yin PF, Yang SQ (2018) Experimental investigation of the strength and failure behavior of layered sandstone under uniaxial compression and Brazilian testing. Acta Geophys 4(66):585–605

Zhang D, Ranjith PG, Perera MSA (2016) The brittleness indices used in rock mechanics and their application in shale hydraulic fracturing: a review. J Pet Sci Eng 143:158–170